

Enabling Visual Action Planning for Object Manipulation through Latent Space Roadmap

Martina Lippi^{*1,2}, Petra Poklukar^{*1}, Michael C. Welle^{*1}, Anastasiia Varava¹,
Hang Yin¹, Alessandro Marino³, and Danica Kragic¹

Abstract—We present a framework for visual action planning of complex manipulation tasks with high-dimensional state spaces, focusing on manipulation of deformable objects. We propose a Latent Space Roadmap (LSR) for task planning, a graph-based structure capturing globally the system dynamics in a low-dimensional latent space. Our framework consists of three parts: (1) a Mapping Module (MM) that maps observations, given in the form of images, into a structured latent space extracting the respective states, that generates observations from the latent states, (2) the LSR which builds and connects clusters containing similar states in order to find the latent plans between start and goal states extracted by MM, and (3) the Action Proposal Module that complements the latent plan found by the LSR with the corresponding actions. We present a thorough investigation of our framework on two simulated box stacking tasks and a folding task executed on a real robot.

I. INTRODUCTION

In task and motion planning, it is common to assume that the geometry of the scene is given as input to the planner. In contrast, modern representation learning methods are able to automatically extract state representations directly from high-dimensional raw observations, such as images or video sequences [1]. This is especially useful in complex scenarios where explicit analytical modeling of states is challenging, such as in manipulation of *highly deformable* objects which is recently gaining increasing attention by the research community [2], [3].

Unsupervised State Representation Learning. Given raw observations, state representation learning is commonly performed in an unsupervised way using for example Autoencoders (AEs) [4], [5] or Variational Autoencoders (VAEs) [6], [7]. In these frameworks, two neural networks – an encoder and a decoder – are jointly trained to embed the input observation into a low-dimensional latent space, and to reconstruct it given a latent sample. The resulting latent space can be used as a low-dimensional representation of the state space, where the encoder acts as a map from a high-dimensional observation (an image) into the lower-dimensional state (a latent vector).

However, to be useful for planning, it is desirable to have a particular structure in the latent space: states that are similar should be encoded close to each other, while different states should be separated. Such information does not always coincide with the similarity of the respective

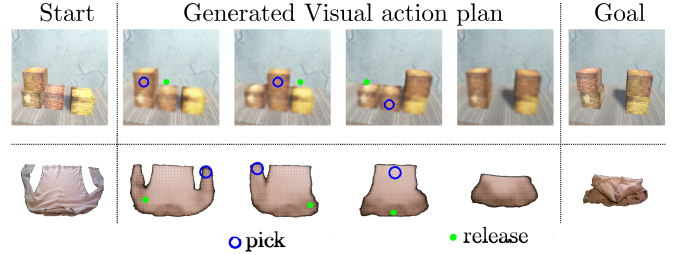


Fig. 1: Examples of visual action plans for a stacking (top) and a folding (bottom) task.

images: two observations can be significantly different with respect to a pixel-wise metric due to task-irrelevant factors of variation such as changes in the lighting conditions and texture, while the underlying state of the system (e.g., the shape and the pose of the objects) may be identical. The opposite is also possible: two observations may be relatively close in the image space, because the respective change in the configuration of the scene does not significantly affect the pixel-wise metric, while from the task planning perspective the two states are fundamentally different.

Challenges of State Representation Learning for Planning.

For planning, the system dynamics should also be captured in the latent space. We therefore identify three main challenges when modeling the state space representation for planning: *i*) it needs to be low dimensional, while containing the relevant information from high-dimensional observations; *ii*) it needs to properly reflect similarities between states; and *iii*) it needs to efficiently capture feasible transitions between states allowing to perform complex tasks such as deformable object manipulation.

In this work, we address *i*) by extracting the low-dimensional states directly from images of the scene through a Mapping Module (MM). For this, we deploy a VAE framework and compare it to AE.

We address *ii*) by explicitly encouraging the encoder network to map the observations that correspond to different states further away from each other despite their visual similarity. This is done by providing a weak supervision signal: we record a small number of actions between observation pairs, and mark the observations as “same” or “different” depending on whether or not an action is needed to bring the system from one state to the successor one. We use this action information in an additional loss term to structure the latent space accordingly.

^{*}These authors contributed equally (listed in alphabetical order)

¹KTH Royal Institute of Technology, Stockholm, Sweden

²University of Roma Tre, Rome, Italy

³University of Cassino and Southern Lazio, Cassino, Italy

Finally, we tackle *iii*) by building the Latent Space Roadmap (LSR), which is a graph-based structure in the latent space used to plan a manipulation sequence given a start and goal image of the scene. The nodes of this graph are associated with the system states, and the edges model the actions connecting them. For example, as shown in Fig. 1, these actions can correspond to moving a box or folding a shirt. We identify the regions containing the same underlying states using hierarchical clustering [8] which accounts for differences in shapes and densities of these regions. The extracted clusters are then connected using the weak supervision signals. Finally, the action specifics are obtained from the Action Proposal Module (APM). In this way, we capture the global dynamics of the state space in a data-efficient manner without explicit state labels, which allows us to learn a state space representation for complex *long-horizon* tasks.

Contributions and Outline. Our contributions can be summarized as follows: *i*) we define the Latent Space Roadmap that enables to generate visual action plans based on weak supervision; *ii*) we introduce an augmented loss function with dynamic parameter to favourably structure the latent space; *iii*) we validate our framework on simulated box stacking tasks and on a T-shirt folding task performed on a real robot. Complete details can be found on the website¹.

This work is a revised and extended version of our earlier conference paper [9], where we first introduced the notion of Latent Space Roadmap. The main novelties of the present work with respect to [9] are:

- 1) Extension of the LSR building algorithm with an outer optimisation loop improving its performance;
- 2) New training approach for the MM with a dynamic adjustment of the key hyperparameter used in the additional loss term;
- 3) Large scale simulation experiments investigating the effect of the additional loss term and hyperparameter choices;
- 4) Comparison with other potentially suitable clustering algorithms used to build the LSR;
- 5) Comparison of VAE with AE as possible choice for the MM;
- 6) Comparison of different realizations of the APM;
- 7) Introduction of a more challenging box stacking task enabling a thorough ablation study on all components of our framework;
- 8) Comparison of the improved framework with its predecessor [9] on the T-shirt folding task performed on a real robot.

The remainder of the paper is organized as follows: we first present the related work in Sec. II and compare it to our approach. We then formally state the problem addressed in this work and introduce the notation in Sec. III. Next, we provide an overview of the proposed approach in Sec. IV and details of the respective three modules in Secs. V, VI and VII. Finally, we show the effectiveness of our method with two versions

of a simulated box stacking task in Sec. VIII and with a real-world folding task in Sec. IX.

II. RELATED WORK

The state representation, in terms of shape and poses of objects in the robot’s workspace, is generally assumed to be known in task and motion planning and represents an input to the planner. As an example, robot and grasping knowledge is exploited in [10] to carry out sequential manipulation tasks, while semantic maps are designed in [11] to integrate spacial and semantic information and perform task planning. In addition, the notion of belief space, representing all possible distributions over the robot state space, is introduced in [12] to tackle partially observable control problems. Alternatively, sampling-based planning approaches, such as Rapidly exploring Random Tree (RRT) or Rapidly exploring Dense Tree (RDT) [13], can be adopted to probe the state space when an explicit representation of it is difficult to achieve.

However, traditional planning approaches, like the ones mentioned above, are generally prone to fail when high-dimensional states, such as images, are involved in the system [14]. For this reason, data-driven low-dimensional latent space representations for planning are gaining increasing attention, which, nonetheless, introduce problems to properly capture the global structure and dynamics of the system, as discussed in Sec. I. To tackle these, imitation learning can be leveraged as in [15], [16]. In particular, a latent space Universal Planning Network is designed in [15] to embed differentiable planning policies. The process is learned in an end-to-end fashion from imitation learning and gradient descent is used to find optimal trajectories. A controller based on random forests is then built in [16] to perform cloth manipulation assuming the presence of optimal demonstrations provided by experts. Alternatively, a motion planning network with active learning procedure is developed in [17] to reduce the data for training and actively ask for expert demonstrations only when needed. In particular, the approach relies on an encoder network, that maps the robot surrounding environment in a low-dimensional state space, and on a prediction network, that is iteratively queried to provide states in the planned path on the basis of environment encoding and the robot initial and goal states.

In contrast to imitation learning methods, self-supervised learning approaches can be applied to mitigate the reduced generalization capabilities of the former at the expense of a costly data collection phase. Although physical simulators such as MuJoCo [18] can in principle be employed for this phase, simulating complex dynamics of deformable objects/robot interaction remains an open problem. Therefore, real robotic platforms should be used for collecting large amounts of training data, undermining the applicability of self-supervised approaches. This problem becomes even more severe when dealing with long-horizon task planning, where the range of possible variations in the state space is large.

In this context, a framework for global search in latent space is designed in [19] and is based on three components: *i*) a latent state representation, *ii*) a network to approximate the latent space dynamics, and *iii*) a collision checking network. Motion planning is then performed directly in the latent space by an

¹<https://visual-action-planning.github.io/lsr-v2/>

RRT-based algorithm. A Deep Planning Network is proposed in [20] to perform continuous control tasks where a transition model, an observation model and a reward model in the latent space are learned and are then exploited to maximize an expected reward function. The manipulation of a deformable rope from an initial start state to a desired goal state is analyzed in [21]. To this aim, it builds upon [22] and [23], where 500 hours worth of data collection are used to learn the rope inverse dynamics, and then produces an *understandable* visual foresight plan containing the intermediate steps to deform the rope using a Context Conditional Causal InfoGAN (C^3 IGAN). Goal-conditioning is then introduced in [24] to carry out long-horizon visual planning by reducing the search space and performing hierarchical optimization. Visual foresight is also realized in [25] where a video prediction model based on Long-Short Term Memory blocks is employed to predict stochastic pixel flow from frame to frame. Trained on video, action and state sequences, the model provides an RGB prediction of the scene that is then used to perform visual model predictive control. The data was collected using ten identical real world setups with different camera angles. In this work, instead of performing imitation learning from experts or exploring the latent space in a self-supervised manner, we leverage a weak supervision given by demonstrated actions in the dataset to capture the global structure of the state space and its dynamics in a data-efficient manner.

Finally, the idea of employing graphs as data representation has recently been investigated in several works. In [26], the authors introduce contrastive learning for structured world models. An end-to-end framework is presented that uses a Convolutional Neural Network (CNN) extractor to segment objects from the given scene observations and a Multi-Layer Perceptron encoder to produce their representations. A graph neural network is then learned to model the relations and transitions given the representations of objects in the scene. Moreover, as graphs naturally decompose a long-horizon task into short-horizon tasks, authors of [27] improve reinforcement learning performance on long-horizon tasks by building a graph whose nodes are the states contained in the replay buffer. In this work, we use graphs to capture the structure and the dynamics of the system, where nodes represent states of the system and edges the possible transitions between them.

III. PROBLEM STATEMENT AND NOTATION

The goal of visual action planning, also referred to as “*visual planning and acting*” in [21], can be formulated as follows: given start and goal images, generate a path as a sequence of images representing intermediate states and compute dynamically valid actions between them. We now formalize the problem and provide notation in Table I.

Let \mathcal{I} be the space of all possible observations of the system’s states represented as images with fixed resolution and let \mathcal{U} be the set of possible control inputs or actions.

Definition 1: A *visual action plan* consists of a *visual plan* represented as a sequence of images $P_I = \{I_{start} = I_0, I_1, \dots, I_N = I_{goal}\}$ where $I_{start}, I_{goal} \in \mathcal{I}$ are images capturing the underlying start and goal states of the system, respectively, and an *action plan* represented as a sequence of

Variable	Meaning
\mathcal{I}	Space of observations, <i>i.e.</i> , images
\mathcal{U}	Space of actions
\mathcal{Z}	Low-dimensional latent space
P_I, P_u, P_z	Planned sequence of images, actions and latent states from assigned start and goal observations, respectively
\mathcal{Z}_{sys}^i	Covered region i of the latent space
\mathcal{Z}_{sys}	Overall covered region of the latent space
ρ	Specifics of the action that took place between two images I_1 and I_2
$\mathcal{T}_I, \mathcal{T}_z$	Datasets containing image tuples (I_1, I_2, ρ) and their embeddings (z_1, z_2, ρ) , respectively
ξ	Latent mapping function from \mathcal{I} to \mathcal{Z}
ω	Observation generator function from \mathcal{Z} to \mathcal{I}
d_m	Minimum distance encouraged among action pairs in the latent space
p	Metric L_p
τ	Clustering threshold for LSR building
c_{max}	Maximum number of connected components of the LSR
ε_z	The ε -neighbourhood of a covered state z containing same covered states
ε^i	ε_z associated with all the states in the covered region \mathcal{Z}_{sys}^i , <i>i.e.</i> $\varepsilon^i = \varepsilon_z \forall z \in \mathcal{Z}_{sys}^i$

Table I: Main notations introduced in the paper.

actions $P_u = \{u_0, u_1, \dots, u_{N-1}\}$ where $u_n \in \mathcal{U}$ generates a transition between consecutive states contained in the observations I_n and I_{n+1} for each $n \in \{0, \dots, N-1\}$.

To retrieve the underlying states represented in the observations as well as to reduce the complexity of the problem we map \mathcal{I} into a lower-dimensional latent space \mathcal{Z} such that each observation $I_n \in \mathcal{I}$ is encoded as a point $z_n \in \mathcal{Z}$ extracting the state of the system captured in the image I_n . We call such map *latent mapping* and denote it by $\xi : \mathcal{I} \rightarrow \mathcal{Z}$. In order to generate visual plans, we additionally assume the existence of a mapping $\omega : \mathcal{Z} \rightarrow \mathcal{I}$ called *observation generator*.

Let $\mathcal{T}_I = \{I_1, \dots, I_M\} \subset \mathcal{I}$ be a finite set of input observations inducing a set of *covered states* $\mathcal{T}_z = \{z_1, \dots, z_M\} \subset \mathcal{Z}$, *i.e.*, $\mathcal{T}_z = \xi(\mathcal{T}_I)$. In order to identify a set of unique covered states, we make the following assumption on \mathcal{T}_z .

Assumption 1: Let $z \in \mathcal{T}_z$ be a covered state. Then there exists $\varepsilon_z > 0$ such that any other state z' in the ε_z -neighborhood $N_{\varepsilon_z}(z)$ of z can be considered as the same underlying state.

This allows both generating a valid visual action plan and taking into account the uncertainty induced by imprecisions in action execution. Let

$$\mathcal{Z}_{sys} = \bigcup_{z \in \mathcal{T}_z} N_{\varepsilon_z}(z) \subset \mathcal{Z} \quad (1)$$

be the union of ε_z -neighbourhoods of the covered states $z \in \mathcal{T}_z$. Given \mathcal{Z}_{sys} , a visual plan can be computed in the latent space using a *latent plan* $P_z = \{z_{start} = z_0, z_1, \dots, z_N = z_{goal}\}$, where $z_n \in \mathcal{Z}_{sys}$, which is then decoded with the observation generator ω into a sequence of images.

To obtain a valid visual plan, we study the structure of the

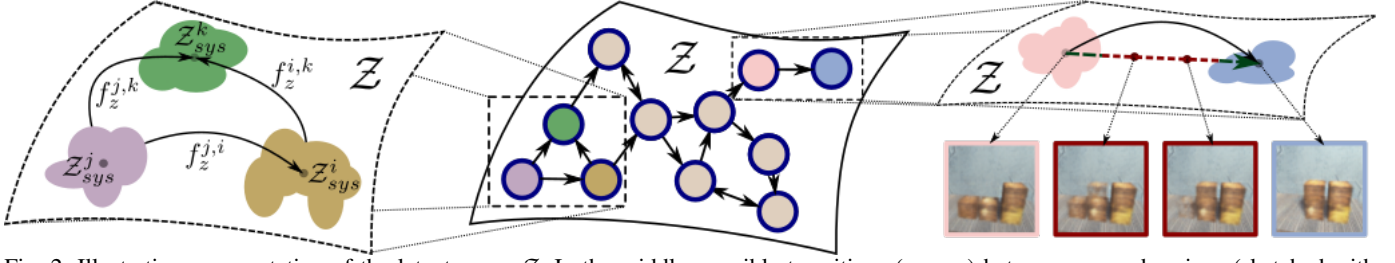


Fig. 2: Illustrative representation of the latent space \mathcal{Z} . In the middle, possible transitions (arrows) between covered regions (sketched with circles) are shown. On the left, details of the covered regions with different shapes and their representative points are provided. On the right, observations from a box stacking tasks are shown. More specifically, the ones obtained from the covered regions (marked in pink and blue) contain meaningful states of the task, while the ones generated from not covered regions (marked in red) show fading boxes that do not represent possible states of the system.

space \mathcal{Z}_{sys} which is in general not path-connected. As we show in Fig. 2 on the right, linear interpolation between two states z_1 and z_2 in \mathcal{Z}_{sys} may result in a path containing points from $\mathcal{Z} - \mathcal{Z}_{sys}$ that do not correspond to covered states of the system and are therefore not guaranteed to be meaningful. To formalize this, we define an equivalence relation in \mathcal{Z}_{sys}

$$z \sim z' \iff z \text{ and } z' \text{ are path-connected in } \mathcal{Z}_{sys}, \quad (2)$$

which induces a partition of the space \mathcal{Z}_{sys} into m equivalence classes $[z_1], \dots, [z_m]$. Each equivalence class $[z_i]$ represents a path-connected component of \mathcal{Z}_{sys}

$$\mathcal{Z}_{sys}^i = \bigcup_{z \in [z_i]} N_{\varepsilon_z}(z) \subset \mathcal{Z}_{sys} \quad (3)$$

called *covered region*. To connect the covered regions, we define a set of transitions between them:

Definition 2: A transition function $f_z^{i,j} : \mathcal{Z}_{sys}^i \times \mathcal{U} \rightarrow \mathcal{Z}_{sys}^j$ maps any point $z \in \mathcal{Z}_{sys}^i$ to an equivalence class representative $z_{sys}^j \in \mathcal{Z}_{sys}^j$, where $i, j \in \{1, 2, \dots, m\}$ and $i \neq j$.

Equivalence relation (2) and Assumption 1 imply that two distinct observations I_1 and I_2 which are mapped into the same covered region \mathcal{Z}_{sys}^i contain the same underlying state of the system, and can be represented by the same equivalence class representative z_{sys}^i . Given a set of covered regions \mathcal{Z}_{sys}^i in \mathcal{Z}_{sys} and a set of transition functions connecting them we can approximate the global transitions of \mathcal{Z}_{sys} as shown in Fig. 2 on the left. To this end, we define a Latent Space Roadmap (see Fig. 2 in the middle):

Definition 3: A Latent Space Roadmap is a directed graph $\text{LSR} = (\mathcal{V}_{\text{LSR}}, \mathcal{E}_{\text{LSR}})$ where each vertex $v_i \in \mathcal{V}_{\text{LSR}} \subset \mathcal{Z}_{sys}$ for $i \in \{1, 2, \dots, m\}$ is an equivalence class representative of the covered region $\mathcal{Z}_{sys}^i \subset \mathcal{Z}_{sys}$, and an edge $e_{i,j} = (v_i, v_j) \in \mathcal{E}_{\text{LSR}}$ represents a transition function $f_z^{i,j}$ between the corresponding covered regions \mathcal{Z}_{sys}^i and \mathcal{Z}_{sys}^j for $i \neq j$. Moreover, weakly connected components of an LSR are called *graph-connected components*.

IV. METHODOLOGY

We first present the structure of the training dataset and then provide an overview of the approach.

A. Training Dataset

We consider a training dataset \mathcal{T}_I consisting of generic tuples of the form (I_1, I_2, ρ) where $I_1 \subset \mathcal{I}$ is an image of the start state, $I_2 \subset \mathcal{I}$ an image of the successor state, and ρ

a variable representing the action that took place between the two observations. Here, an action is considered to be a *single* transformation that produces any consecutive state represented in I_2 different from the start state in I_1 , i.e., ρ cannot be a composition of several transformations. On the contrary, we say that no action was performed if images I_1 and I_2 are observations of the same state, i.e., if $\xi(I_1) \sim \xi(I_2)$ with respect to the equivalence relation (2). The variable $\rho = (a, u)$ consists of a binary variable $a \in \{0, 1\}$ indicating whether or not an action occurred as well as a variable u containing the task-dependent action-specific information. The latter, if available, is used to infer the transition functions $f_z^{i,j}$. We call a tuple $(I_1, I_2, \rho = (1, u))$ an *action pair* and $(I_1, I_2, \rho = (0, u))$ a *no-action pair*. For instance, Fig. 4 shows an example of an action pair (top row) and a no-action pair (bottom row) for the folding task. In this case, the action specifics u contain the pick and place coordinates to achieve the transition from the state captured by I_1 to the state captured by I_2 , while the no-action pair images are *different* observations of the same underlying state of the system represented by slight perturbations of the sleeves. When the specifics of an action u are not needed, we omit them from the tuple notation and simply write (I_1, I_2, a) . By abuse of notation, we sometimes refer to an observation I contained in any of the training tuples as $I \in \mathcal{T}_I$. Finally, we denote by \mathcal{T}_z the encoded training dataset \mathcal{T}_I consisting of latent tuples (z_1, z_2, ρ) obtained from the input tuples $(I_1, I_2, \rho) \in \mathcal{T}_I$ by encoding the inputs I_1 and I_2 into the latent space \mathcal{Z}_{sys} with the latent mapping ξ . The obtained states $z_1, z_2 \in \mathcal{Z}_{sys}$ are called *covered states*.

Remark 1: The dataset \mathcal{T}_I is not required to contain all possible action pairs of the system but only a subset of them that sufficiently cover the dynamics, which makes our approach data efficient as we show in Sec. VIII-B5.

B. System Overview

Generation of visual action plans consists of three components, see Fig. 3:

- **Mapping Module (MM)** used to both extract a low-dimensional representation of a state represented by a given observation, and to generate an exemplary observation from a given latent state;
- **Latent Space Roadmap (LSR)** built in the low dimensional latent space and used to perform planning;

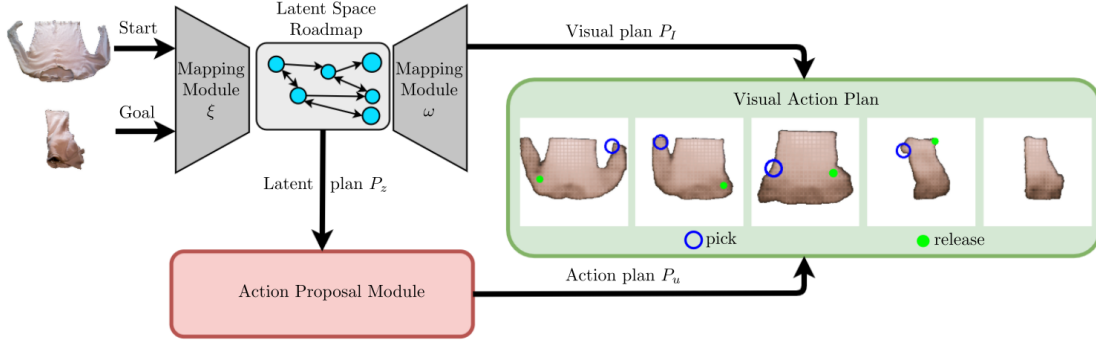


Fig. 3: Overview of the proposed method. Start and goal images (on the left) are mapped to the latent space \mathcal{Z} by the latent mapping ξ of the Mapping Module. A latent plan is then found with the Latent Space Roadmap (cyan circles and arrows) and is decoded to a visual plan using the observation generator ω of the Mapping Module. The Action Proposal Module (red) proposes suitable actions to achieve the transitions between states in the visual plan. The final result is a *visual action plan* (green) from start to goal.

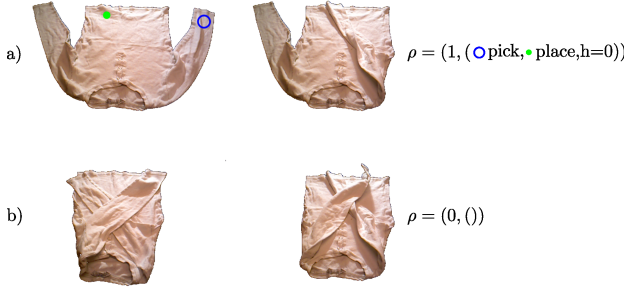


Fig. 4: Example of action (a) and no-action (b) pairs for the folding task.

- **Action Proposal Module (APM)** used to predict action specifics for executing a latent plan found by the LSR.

The MM consists of the latent mapping $\xi : \mathcal{I} \rightarrow \mathcal{Z}$ and the observation generator $\omega : \mathcal{Z} \rightarrow \mathcal{I}$. Given an observation I , ξ extracts a lower-dimensional representation z of the underlying state of the system. Using the observation generator ω , we can then obtain an exemplary observation I' , possibly different from I , corresponding to z . We realize the mappings ξ and ω with the encoder and decoder networks of a VAE trained with an augmented loss function. Consequently, the latent space of the trained VAE is the realization of the space \mathcal{Z} .

To find a visual plan between a given start observation I_{start} and goal observation I_{goal} , the latent mapping ξ first extracts the corresponding start and goal states z_{start} and z_{goal} , respectively. Note that ideally the mapping ξ should perfectly extract the underlying state of the system, *i.e.*, different observations containing the same state should be mapped into the same latent point. However, ξ is generally only an *approximation* of the unknown true latent embedding, implying that different observations containing the same state could be mapped to different latent points. In order to perform planning in the latent space \mathcal{Z} , we thus build the LSR which is a graph-based structure identifying the latent points belonging to the same underlying state and approximating the system dynamics. This enables finding the latent plans P_z between the extracted states z_{start} and z_{goal} . For the sake of interpretability, latent plans P_z are decoded into visual plans P_I , consisting of a sequence of images, by the observation generator ω .

We complement the generated visual plan with the action plan produced by the APM. It takes a pair (z_i, z_{i+1}) of

consecutive states from the latent plan P_z found by the LSR as inputs, and proposes an action u_i to achieve the desired transition $f_z^{i,i+1}(z_i, u_i) = z_{i+1}$. Applying APM to all consecutive pairs of states in P_z results in an action plan P_u .

The visual action plan produced by the three components can be executed by any suitable framework. If open loop execution is not sufficient for the task, a re-planning step can be added after every action as shown in the T-shirt folding experiments in Section IX.

Remark 2: Our method is able to generate a sequence of actions $\{u_0, \dots, u_{N-1}\}$ to reach a goal state in I_N from a given start state represented by I_0 , even though the tuples in the input dataset \mathcal{T}_I only contain *single* actions u that represent the weak supervision signals.

V. MAPPING MODULE (MM)

The mappings $\xi : \mathcal{I} \rightarrow \mathcal{Z}$ and $\omega : \mathcal{Z} \rightarrow \mathcal{I}$ as well as the low-dimensional space \mathcal{Z} can be realized using any encoder-decoder based algorithms, for example VAEs, AEs or Generative Adversarial Networks (GANs) combined with an encoder network. The primary goal of MM is to find the best possible approximation ξ such that the structure of the extracted states in the latent space \mathcal{Z} resembles the one corresponding to the unknown underlying system. The secondary goal of MM is to learn an observation generator ω which enables visual interpretability of the latent plans. Since the quality of these depends on the structure of the latent space \mathcal{Z} , we leverage the action information contained in the binary variable a of the training tuples (I_1, I_2, a) to improve the quality of the latent space. We achieve this by introducing a contrastive loss term [28] which can be easily added to the loss function of any algorithm used to model the MM.

More precisely, we introduce a general *action* term

$$\mathcal{L}_{action}(I_1, I_2) = \begin{cases} \max(0, d_m - \|z_1 - z_2\|_p) & \text{if } a = 1 \\ \|z_1 - z_2\|_p & \text{if } a = 0 \end{cases} \quad (4)$$

where $z_1, z_2 \in \mathcal{Z}_{sys}$ are the latent encodings of the input observations $I_1, I_2 \in \mathcal{T}_I$, respectively, d_m is a hyperparameter, and the subscript $p \in \{1, 2, \infty\}$ denotes the metric L_p . The action term \mathcal{L}_{action} naturally imposes the formulation of the covered regions \mathcal{Z}_{sys}^i in the latent space. On one hand, it encodes identical states contained in the no-action pairs

close by. On the other hand, it encourages different states to be encoded in separate parts of the latent space via the hyperparameter d_m .

As we experimentally show in Sec. VIII-B1, the choice of d_m has a substantial impact on the latent space structure. Therefore, we propose to learn its value *dynamically* during the training of the MM. In particular, d_m is increased until the separation of action and no-action pairs is achieved. Starting from 0 at the beginning of the training, we increase d_m by Δd_m every k th epoch as long as the maximum distance between no-action pairs is larger than the minimum distance between action pairs. The effect of dynamically increasing d_m is shown in Fig. 5 where we visualize the distance $\|z_1 - z_2\|_1$ between the latent encodings of every action training pair (in blue) and no-action training pair (in green) obtained at various epochs during training on a box stacking task. It can be clearly seen that the parameter d_m is increased as long as there is an intersection between action and no-action pairs. Detailed investigation of this approach as well as its positive effects on the structure of the latent space are provided in Sec. VIII-B1. Note that the dynamic adaptation of the parameter d_m eliminates the need to predetermine its value as in our previous work [9].

We use a VAE such that its latent space represents the space \mathcal{Z} , while the encoder and decoder networks realize the mappings ξ and ω , respectively. We validate this choice in Sec. VIII-B4 by comparing it to AE. In the following, we first provide a brief summary of the VAE framework [6], [7] and then show how the action term can be integrated into its training objective. Let $I \subset \mathcal{T}_I$ be an input image, and let z denote the unobserved latent variable with prior distribution $p(z)$. The VAE model consists of encoder and decoder neural networks that are jointly optimized to represent the parameters of the approximate posterior distribution $q(z|I)$ and the likelihood function $p(I|z)$, respectively. In particular, VAE is trained to minimize

$$\mathcal{L}_{vae}(I) = E_{z \sim q(z|I)}[\log p(I|z)] + \beta \cdot D_{KL}(q(z|I) || p(z)) \quad (5)$$

with respect to the parameters of the encoder and decoder neural networks. The first term influences the quality of the reconstructed samples, while the second term, called Kullback-Leibler (KL) divergence term, regulates the structure of the latent space. The trade-off between better reconstructions or a more structured latent space is controlled by the parameter β , where using a $\beta > 1$ favors the latter [29], [30]. The action term (4) can be easily added to the VAE loss (5) as follows:

$$\mathcal{L}(I_1, I_2) = \frac{1}{2}(\mathcal{L}_{vae}(I_1) + \mathcal{L}_{vae}(I_2)) + \gamma \cdot \mathcal{L}_{action}(I_1, I_2) \quad (6)$$

where $I_1, I_2 \subset \mathcal{T}_I$ and the parameter γ controls the influence of the distances among the latent encodings on the latent space structure. Note that the same procedure applies for integrating the action term (4) into any other framework that models the MM.

VI. LATENT SPACE ROADMAP (LSR)

The Latent Space Roadmap, defined in *Definition 3*, is built in the latent space \mathcal{Z} obtained from the MM. LSR is a

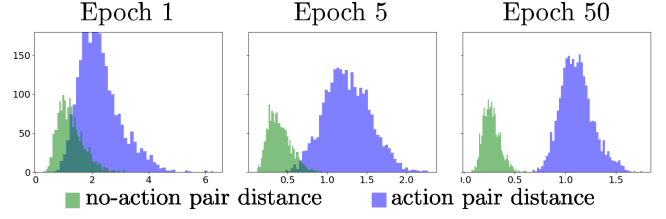


Fig. 5: An example showing histograms of distances $\|z_1 - z_2\|_1$ for latent action (in blue) and no-action pairs (in green) obtained at epochs 1, 5 and 50 during the training of VAE on the hard box stacking task (more details in Sec. VIII). The figure shows the separation of the action and no-action distances induced by dynamically increasing the minimum distance d_m in \mathcal{L}_{action} .

graph that enables planning in the latent space which identifies sets of latent points associated with the same underlying state and viable transitions between them. Each node in the roadmap is associated with a covered region \mathcal{Z}_{sys}^i . Two nodes are connected by an edge if there exists an action pair $(I_1, I_2, \rho = (1, u_1))$ in the training dataset \mathcal{T}_I such that the transition $f_z^{1,2}(z_1, u_1) = z_2$ is achieved in \mathcal{Z}_{sys} .

The LSR building procedure is summarized in Algorithm 1 and discussed in Sec. VI-A. It relies on a clustering algorithm that builds the LSR using the encoded training data \mathcal{T}_z and a specified metric L_p as inputs. The input parameter τ is inherited from the clustering algorithm and we automatically determine it using the procedure described in Sec. VI-B.

Algorithm 1 LSR building

Require: Dataset \mathcal{T}_z , metric L_p , clustering threshold τ

Phase 1

- 1: init graph $\mathcal{G} = (\mathcal{V}, \mathcal{E}) := (\{\}, \{\})$
- 2: **for each** $(z_1, z_2, a) \in \mathcal{T}_z$ **do**
- 3: $\mathcal{V} \leftarrow$ create nodes z_1, z_2
- 4: **if** $a = 1$ **then**
- 5: $\mathcal{E} \leftarrow$ create edge (z_1, z_2)

Phase 2

- 1: $M \leftarrow$ Average-Agglomerative-Clustering(\mathcal{T}_z, L_p) [8]
- 2: $\mathcal{W} \leftarrow$ get-Disjoint-Clusters(M, τ)
- 3: $\mathcal{Z}_{sys} \leftarrow \{\}$
- 4: **for each** $\mathcal{W}^i \in \mathcal{W}$ **do**
- 5: $\mathcal{E}^i \leftarrow$ get-Cluster-Epsilon(\mathcal{W}^i)
- 6: $\mathcal{Z}_{sys}^i := \cup_{w \in \mathcal{W}^i} N_{\mathcal{E}^i}(w)$
- 7: $\mathcal{Z}_{sys} := \mathcal{Z}_{sys} \cup \{\mathcal{Z}_{sys}^i\}$

Phase 3

- 1: init graph LSR = $(\mathcal{V}_{LSR}, \mathcal{E}_{LSR}) := (\{\}, \{\})$
- 2: **for each** $\mathcal{Z}_{sys}^i \in \mathcal{Z}_{sys}$ **do**
- 3: $w^i := \frac{1}{|\mathcal{W}^i|} \sum_{w \in \mathcal{W}^i} w$
- 4: $z_{sys}^i := \operatorname{argmin}_{z \in \mathcal{Z}_{sys}^i} \|z - w^i\|_p$
- 5: $\mathcal{V}_{LSR} \leftarrow$ create node z_{sys}^i
- 6: **for each edge** $e = (v_1, v_2) \in \mathcal{E}$ **do**
- 7: find $\mathcal{Z}_{sys}^i, \mathcal{Z}_{sys}^j$ containing v_1, v_2 , respectively
- 8: $\mathcal{E}_{LSR} \leftarrow$ create edge (z_{sys}^i, z_{sys}^j)

return LSR

A. LSR Building

Algorithm 1 consists of three phases. In Phase 1 (lines 1.1 – 1.5), we build a *reference* graph $\mathcal{G} = (\mathcal{V}, \mathcal{E})$ induced by \mathcal{T}_z and visualized in the left part of Fig. 6. Its set of vertices \mathcal{V} is the

set of all the latent states in \mathcal{T}_z , while edges exist only among the latent action pairs. It serves as a look-up graph to preserve the edges that later induce the transition functions $f_z^{i,j}$.

In Phase 2, we identify the covered regions $\mathcal{Z}_{sys}^i \subset \mathcal{Z}_{sys}$. We achieve this by first clustering the training samples and then retrieving the covered regions from these clusters. We start by performing agglomerative clustering [8] on the encoded dataset \mathcal{T}_z (line 2.1). Agglomerative clustering is a hierarchical clustering scheme that starts from single nodes of the dataset and merges the closest nodes, according to a dissimilarity measure, step by step until only one node remains. It results in a *stepwise dendrogram* M , depicted in the middle part of Fig. 6, which is a tree structure visualizing the arrangement of data points in clusters with respect to the level of dissimilarity between them. We choose to measure this inter-cluster dissimilarity using the *unweighted average* distance between points in each cluster, a method also referred to as UPGMA [31]. More details about other possible clustering algorithms and dissimilarity measures are discussed in Sec. VIII-C. Next, the dissimilarity value τ , referred to as *clustering threshold*, induces the set of disjoint clusters \mathcal{W} , also called *flat* or *partitional* clusters [32], [33], from the stepwise dendrogram M [8] (line 2.2). Points in each cluster \mathcal{W}^i are then assigned a uniform ε^i (line 2.5), *i.e.* the neighbourhood size from Assumption 1 of each point $z \in \mathcal{W}^i$ is $\varepsilon_z = \varepsilon^i$. We discuss the definition of the ε^i value at the end of this phase. The union of the ε^i -neighbourhoods of the points in \mathcal{W}^i then forms the covered region \mathcal{Z}_{sys}^i (line 2.6). Illustrative examples of covered regions obtained from different values of τ are visualized on the right side of Fig. 6 using various colors. The optimization of τ is discussed in Sec. VI-B. The result of this phase is the set of the identified covered regions $\mathcal{Z}_{sys} = \{\mathcal{Z}_{sys}^i\}$ (line 2.7).

We propose to approximate ε^i as

$$\varepsilon^i = \mu^i + \sigma^i \quad (7)$$

where μ^i and σ^i are the mean and the standard deviation of the distances $\|z_j^i - z_k^i\|_p$ among all the training pairs $(z_j^i, z_k^i) \in \mathcal{T}_z$ belonging to the i th cluster. The approximation in (7) allows to take into account the cluster density such that denser clusters get lower ε^i . In contrast to our previous work [9], we now enable clusters to have different ε values. We validate the approximation (7) in Secs. VIII-C4 and IX-C1 where we analyze the covered regions identified by the LSR.

In Phase 3, we build the LSR $= (\mathcal{V}_{LSR}, \mathcal{E}_{LSR})$. We first compute the mean value w^i of all the points in each cluster \mathcal{W}^i (line 3.3). As the mean itself might not be contained in the corresponding path-connected component, we find the equivalence class representative $z_{sys}^i \in \mathcal{Z}_{sys}^i$ that is the closest (line 3.4). The found representative then defines a node $v_i \in \mathcal{V}_{LSR}$ representing the covered region \mathcal{Z}_{sys}^i (line 3.5). Lastly, we use the set of edges \mathcal{E} in the reference graph built in Phase 1 to infer the transitions $f_z^{i,j}$ between the covered regions identified in Phase 2. We create an edge in LSR if there exists an edge in \mathcal{E} between two vertices in \mathcal{V} that were allocated to different covered regions (lines 3.6 – 3.8). The right side of Fig. 6 shows the final LSRs, obtained with different values of the clustering threshold τ .

Note that, as in the case of the VAE (Sec. V), no action-specific information u is used in Algorithm 1 but solely the binary variable a indicating the occurrence of an action.

B. Optimisation of LSR Clustering Threshold τ

The clustering threshold τ , introduced in Phase 2 of Algorithm 1, heavily influences the number and form of the resulting clusters. Since there is no inherent way to prefer one cluster configuration over another, finding its optimal value is a non-trivial problem and subject to ongoing research [34], [35], [36]. However, in our case, since the choice of τ subsequently influences the resulting LSR, we can leverage the information about the latter in order to optimize τ . Details are provided in the following.

As illustrated in Fig. 6, the number of vertices and edges in LSR_{τ_i} changes with the choice of τ_i . Moreover, the resulting LSRs can have different number of *graph*-connected components. For example, LSR_{τ_1} in Fig. 6 has 2 graph-connected components, while LSR_{τ_2} and LSR_{τ_3} have only a single one. Ideally, we want to obtain a graph that exhibits both good connectivity which best approximates the true underlying dynamics of the system, and has a limited number of graph-connected component. Intuitively, high number of edges increases the possibility to find latent paths from start to goal state. At the same time, this possibility is decreased when the graph is fragmented into several isolated components, which is why we are also interested in limiting the maximum number of graph-connected components.

While we cannot analyze the clusters themselves, we can evaluate information captured by the LSR that correlates with the performance of the task, *i.e.*, we can assess a graph by the number of edges and graph-connected components it exhibits as discussed above. This induces an objective which we can use to optimize the value of the clustering threshold τ . We formulate it as

$$\psi(\tau, c_{\max}) = \begin{cases} |\mathcal{E}_{\text{LSR}_\tau}| & \text{if } c_{\text{LSR}_\tau} \leq c_{\max}, \\ -\infty & \text{otherwise,} \end{cases} \quad (8)$$

where $|\mathcal{E}_{\text{LSR}_\tau}|$ is the cardinality of the set $\mathcal{E}_{\text{LSR}_\tau}$, c_{LSR_τ} represents the number of graph-connected components of the graph LSR_τ induced by τ , and the hyperparameter c_{\max} represents the upper bound on the number of graph-connected components. The optimal τ in a given interval $[\tau_{\min}, \tau_{\max}]$ can be found by any scalar optimization method. In this work, we use Brent's optimization method [37] which maximizes the objective (8)

$$\max_{\tau_{\min} \leq \tau \leq \tau_{\max}} \psi(\tau, c_{\max}). \quad (9)$$

This optimisation procedure is summarized in Algorithm 2. It takes as an input the encoded training data \mathcal{T}_z , the metric L_p , the search interval where the clustering parameter τ is to be optimized, and the upper bound c_{\max} to compute the optimization objective in (8). After initialization of the parameter τ (line 1), for example, by considering the average value of its range, the Brent's optimization loop is performed (lines 2-5). Firstly, the LSR with the current τ is built according to Algorithm 1 (line 3). Secondly, the optimization objective (8) is computed on the obtained LSR_τ (line 4). Thirdly, the

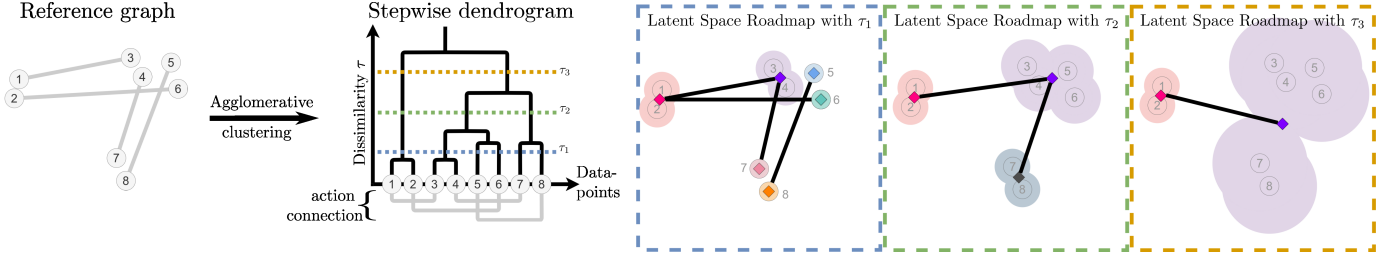


Fig. 6: Illustrative example visualising the LSR building steps and the effect of the clustering threshold τ . On the left is the reference graph built in Phase 1 of Algorithm 1. Middle part visualizes a dendrogram M obtained from the clustering algorithm in Phase 2. On the right, three examples of LSRs are shown together with the covered regions (marked with various colors) corresponding to different clustering thresholds τ (with $\tau_1 < \tau_2 < \tau_3$) chosen from M .

parameter τ as well as the bounds τ_{\min} and τ_{\max} are updated according to [37] (line 5). The optimization loop is performed until the convergence is reached, *i.e.*, until $|\tau_{\max} - \tau_{\min}|$ is small enough according to [37]. Lastly, the optimal τ^* (line 6) is selected for the final LSR_{τ^*} .

Note that even though Algorithm 2 still needs the selection of the hyperparameter c_{\max} , we show in Sec. VIII-C that it is rather robust to the choice of this parameter.

Algorithm 2 LSR input optimization

Require: Dataset \mathcal{T}_z , metric L_p , search interval $[\tau_{\min}, \tau_{\max}]$, c_{\max}

- 1: $\tau \leftarrow \text{init}(\tau_{\min}, \tau_{\max})$
- 2: **while** $|\tau_{\max} - \tau_{\min}|$ not small enough **do**
- 3: $\text{LSR}_{\tau} \leftarrow \text{LSR-building}(\mathcal{T}_z, L_p, \tau)$ [Algorithm 1]
- 4: $\psi \leftarrow \text{Evaluate}(\text{LSR}_{\tau})$ [Eq. (8)]
- 5: $\tau, \tau_{\min}, \tau_{\max} \leftarrow \text{Brent-update}(\psi)$ [37]
- 6: $\tau^* \leftarrow \tau$

return LSR_{τ^*}

C. Visual plan generation

Given a start and goal observation, a trained VAE model and an LSR, the observations are first encoded by ξ into the VAE’s latent space \mathcal{Z} where their closest nodes in the LSR are found. Next, all shortest paths [38] in the LSR between the identified nodes are retrieved. Finally, the equivalence class representatives of the nodes comprising each of the found shortest path compose the respective latent plan P_z , which is then decoded into the visual plan P_I using ω .

VII. ACTION PROPOSAL MODULE (APM)

The final component of our framework is the Action Proposal Module (APM) which is used to complement a latent plan, produced by the LSR, with an action plan that can be executed by a suitable framework. The APM allows to generate the action plans from the extracted low-dimensional state representations rather than high-dimensional observations. The action plan P_u corresponding to a latent plan P_z produced by the LSR is generated sequentially: given two distinct consecutive latent states (z_i, z_{i+1}) from P_z , APM predicts an action u_i that achieves the transition $f^{i,i+1}(z_i, u_i) = z_{i+1}$. Such functionality can be realized by any method that is suitable to model the action specifics of the task at hand.

We model the action specifics with a neural network called Action Proposal Network (APN). We deploy a diamond-shaped multi layer perceptron and train it in a supervised fashion on the latent *action* pairs obtained from the enlarged dataset \mathcal{T}_z as described below. We validate this choice in Sec IX-D where we compare it to different alternatives that produce action plans either by exploiting the LSR or by using the observations as inputs rather than extracted low-dimensional states. The architecture details are reported in the code repository².

The training dataset $\overline{\mathcal{T}}_z$ for the APN is derived from \mathcal{T}_I but preprocessed with the VAE encoder representing the latent mapping ξ . We encode each training *action* pair $(I_1, I_2, \rho = (1, u)) \in \mathcal{T}_I$ into \mathcal{Z} and obtain the parameters μ_i, σ_i of the approximate posterior distributions $q(z|I_i) = N(\mu_i, \sigma_i)$, for $i = 1, 2$. We then sample $2S$ novel points $z_1^s \sim q(z|I_1)$ and $z_2^s \sim q(z|I_2)$ for $s \in \{0, 1, \dots, S\}$. This results in $S+1$ tuples (μ_1, μ_2, ρ) and (z_1^s, z_2^s, ρ) , $0 \leq s \leq S$, where $\rho = (1, u)$ was omitted from the notation for simplicity. The set of all such low-dimensional tuples then forms the APN training dataset $\overline{\mathcal{T}}_z$.

Remark 3: It is worth remarking the two-fold benefit of this preprocessing step: not only does it reduce the dimensionality of the APN training data but also enables enlarging it with novel points by factor $S+1$. Note that the latter procedure is not possible with non-probabilistic realizations of ξ .

VIII. BOX STACKING EXPERIMENTS

We experimentally evaluate our method on two different versions of the simulated box stacking task shown in Fig. 7. The top row shows the setup used in our previous work [9], while the bottom row shows a modified setup where the task of retrieving the underlying state of the system was made harder. This was achieved by using more similar box textures which makes it more difficult to separate the underlying states. We also introduced different lighting conditions which make observations containing the same underlying states look more dissimilar. We refer to the original setup as the *normal stacking* task denoted by ns, and to the modified one as the *hard stacking* task denoted by hs. These two setups enable automatic evaluation of the structure of the latent space \mathcal{Z}_{sys} , the quality of visual plans P_I generated by the LSR and MM, and the quality of action plans P_u predicted by the APN.

² <https://github.com/visual-action-planning/lsr-v2-code>

The hard stacking task was additionally introduced to make the visual action planning more challenging with respect to [9] such that ablation studies on the introduced improvements of our framework can be performed. These are not possible using the normal stacking task since our earlier version of the LSR [9] already outputs perfect visual action plans.

Both setups were developed with the Unity engine [39] and are composed of four boxes with different textures that can be stacked in a 3×3 grid (dotted lines in Fig. 7). A grid cell can be occupied by only one box at a time which can be moved according to the *stacking rules*: i) it can be picked only if there is no other box on top of it, and ii) it can be released only on the ground or on top of another box inside the 3×3 grid. The action-specific information u , shown in Fig. 7, is a pair $u = (p, r)$ of pick p and release r coordinates in the grid modelled by the row and column indices, i.e., $p = (p_r, p_c)$ with $p_r, p_c \in \{0, 1, 2\}$, and equivalently for $r = (r_r, r_c)$.

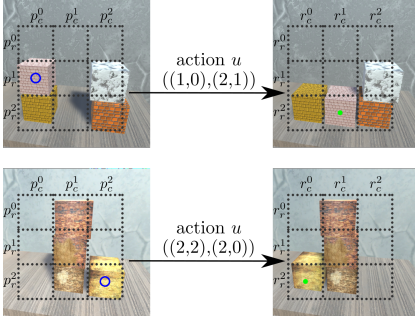


Fig. 7: An example of an action $u = (p, r)$ in the normal (top) and hard (bottom) box stacking tasks. The blue circle shows the picking location p , and the green one the release position r .

In both versions of the dataset, the position of each box in a grid cell was generated by introducing $\sim 17\%$ noise along x and y axes, which was applied when generating both action and no-action pairs. The resulting images have dimension $256 \times 256 \times 3$.

The designed tasks contain exactly 288 different grid configurations, i.e., the specification of which box, if any, is contained in each cell. These 288 grid configurations represent the underlying states in this task. Note that the exact number of underlying states is in general not known. Given a pair of states and the ground truth stacking rules, it is possible to analytically determine whether or not an action is allowed between them. In addition, we can determine the grid configuration associated with an image (i.e., its underlying state) contained in the produced visual plan P_I using classifiers. These were trained on the decoded images and achieved accuracy greater than 99.5% on a holdout dataset composed of 750 samples for both versions of the stacking task. Implementation details can be found on our code repository².

A. Experiment Objectives and Implementation Details

Our experiments are designed to answer the following questions:

- 1) **MM** What is the impact of the action term (4) in the augmented loss function (6) on the structure of the latent space? How do the respective parameters (latent space

dimension, minimum distance, etc.) influence the overall LSR performance? Lastly, how does the VAE framework perform compared to the AE one for modelling the mappings ξ and ω composing the MM?

- 2) **LSR** What is the performance of the LSR and what is the influence of the action term (4) on it? How do the respective LSR parameters (number of components, metric, etc.) and the choice of the clustering algorithm impact the overall LSR performance? How good is the approximation of the covered regions provided by the LSR?
- 3) **APM** What is the performance of the chosen APN model?

In this section, we present the implementation details and introduce the notation used to easily refer to the models in consideration. The complete implementation details for all the models and respective hyperparameters can be found in the configuration files in the code repository². For VAEs (used in MM), each model is annotated by $\text{VAE}_{ld-task-d}$ where ld denotes the dimension of the latent space, $task$ denotes the version of the task and is either *ns* or *hs* for the normal and hard stacking tasks, respectively, and d indicates whether or not the model was trained with the action loss term (4). Here, we use $d = b$ to denote a *baseline* VAE trained with the original VAE objective (5), and $d = L_p$ to denote an *action* VAE trained with the loss function (6) including the action term (4) using metric L_p for $p \in \{1, 2, \infty\}$.

All VAE models used a ResNet architecture [40] for the encoder and decoder networks. They were trained for 500 epochs on a training dataset \mathcal{T}_I , composed of 65% action pairs and 35% no-action pairs. For each combination of parameters ld , $task$, and d , we trained five VAEs initialized with different random seeds. Same seeds were also used to create training and validations splits of the training dataset. The weight β from (5) and (6) was gradually increased from 0 to 2 over 400 epochs following a scheduling procedure², while γ was fixed to 100. In this way, the models were encouraged to first learn to reconstruct the input images and then to gradually structure the latent space. The minimum distance d_m was dynamically increased every fifth epoch starting from 0 using $\Delta d_m = 0.1$ as described in Sec. V. The effect of this dynamic parameter increase is shown in Fig. 5.

For LSR, we denote by $\text{LSR-}L_p$ a graph built using the metric L_p in Algorithm 1. The parameters τ_{\min} and τ_{\max} in the LSR optimization (9) were set to 0 and 3, respectively. Unless otherwise specified, we fixed $ld = 12$ and used L_1 metric for both tasks. Moreover, the number of graph-components c_{\max} in the optimization of the clustering threshold (8) was set to 1 for *ns* and 20 for *hs*. These choices are explained in detail in the following sections.

Given an LSR, we evaluated its performance by measuring the quality of the visual plans found between 1000 randomly selected start and goal observations from an unseen test dataset containing 2500 images. To automatically check the validity of the found paths, we used the classifiers on the observations contained in the visual plans to get the respective underlying states. We then used a validity function² to determine whether or not the state transitions in the paths fulfill all the constraints

determined by the stacking rules. In the evaluation of the planning performance we considered the following quantities: *i*) percentage of cases when all shortest paths from start to goal observations are correct, denoted as *% All*, *ii*) percentage of cases when at least one of the proposed paths is correct, denoted as *% Any*, and *iii*) percentage of correct single transitions in the paths, denoted as *% Trans*. We refer to the *% Any* score in *ii*) as *partial scoring*, and to the combination of scores *i*)-*iii*) as *full scoring*. Moreover, mean and standard deviation values are reported over the 5 different random seeds used to train the VAEs.

For APNs, we use the notation $APN_{ld-task-d}$ analogous to the VAEs. The APN models are trained for 500 epochs on the training dataset $\bar{\mathcal{T}}_z$ obtained following the procedure described in Sec VII using $S = 1$. We used the validation split, corresponding to 15% of $\bar{\mathcal{T}}_z$, to extract the best performing models that were used in the evaluation. Similarly as for LSR, we report the mean and standard deviation of the performance obtained over the 5 random seeds used in the VAE training.

B. MM Analysis

In this section, we demonstrate the positive effect of the action term (4) on the structure of the latent space and justify the choice of the VAE framework for the MM, thus answering the questions listed in point 1) of Sec. VIII-A.

In the first experiment, we investigated the influence of the dynamic minimum distance d_m on the LSR performance. We then studied the structure of the latent space by analyzing the distance between the encodings of the 288 underlying states as well as the separability of the latent points. Next, we compared the LSR performance when modelling MM with an AE framework instead of a VAE. Lastly, we examined how the size of both training dataset and latent dimension affect the overall LSR performance.

1) Influence of dynamic d_m : A key parameter in the action term (4) is the minimum distance d_m encouraged among the action pairs. We considered the hard stacking task and validated the approach proposed in Sec. V, which dynamically increases d_m to separate action and no-action pairs (see Fig. 5), reaching $d_m = 2.3$ at the end of the training. We compared it with (i) the choice in [9] where d_m is fixed and equal to 11.6 which is the average action distance among all the training action pairs measured in the corresponding baseline VAE, and (ii) the case where $d_m = 100$ which is a significantly higher value than the one obtained in (i).

The performance of the LSR, evaluated using full scoring, with respect to the choice of d_m is summarized in Table II. The results show that the dynamic selection of d_m significantly outperforms the other methods for all the scores. *This approach not only eliminates the need for training the baseline VAEs as in [9] but also reaches a value of d_m that obtains a better separation of covered regions \mathcal{Z}_{sys}^i without compromising the optimization of the reconstruction and KL terms.* In fact, as discussed in Sec. V, the reconstruction, KL and action terms in the loss function (5) have distinct influences on the latent space structure which can be in contrast to each other. The proposed dynamic increase of d_m results in a lower d_m value than in [9],

which in turn yields small distances between the action pair states. Such small distances in the action term are desirable as they do not contradict the KL term. This explains why the LSRs with higher values of d_m reach worse performance compared to the dynamic one.

	d_m	% All	% Any	% Trans.
Dynamic (Ours)	-	90.9 ± 3.5	92.1 ± 2.9	95.8 ± 1.3
Baseline [9]	11.6	48.7 ± 40.7	50.7 ± 41.5	72.8 ± 26.0
High	100	0.0	0.0	14.6 ± 2.0

Table II: Comparison of the LSR performance when using different methods for selecting d_m . Top row is our approach where d_m is determined dynamically, middle row is the approach used in [9] where d_m is calculated from the latent action pairs in the baseline VAE, while in the bottom row d_m is set a high value. Results are obtained using $VAE_{12-hs-L_1}$ and $LSR-L_1$.

2) Separation of the states: We investigated the effect of the action loss (4) on the structure of the latent space by analyzing the separation of the latent points $z \in \mathcal{T}_z$ corresponding to different underlying states of the system. Recall that images in \mathcal{T}_I containing the same state will look different because of the introduced positioning noise in both tasks, and different lightning conditions in the case of *hs*.

Let \bar{z}_s be the *centroid* for state s defined as the mean point of the training latent samples $\{z_{s,i}\}_i \subset \mathcal{T}_z$ associated with the state s . Let $d_{intra}(z_{s,i}, \bar{z}_s)$ be the *intra-state* distance defined as the distance between the latent sample i associated with the state s , namely $z_{s,i}$, and the respective centroid \bar{z}_s . Similarly, let $d_{inter}(\bar{z}_s, \bar{z}_p)$ denote the *inter-state* distance between the centroids \bar{z}_s and \bar{z}_p of states s and p , respectively. In the following analysis we considered the models $VAE_{12-ns-L_1}$ and $VAE_{12-ns-L_1}$ for the normal and hard stacking tasks, respectively.

Fig. 8 reports the mean values (bold points) and the standard deviations (thin lines) of the inter- (in blue) and intra-state (in orange) distances for each state $s \in \{1, \dots, 288\}$ in the normal stacking task when using the baseline model $VAE_{12-ns-b}$ (top) and the action model $VAE_{12-ns-L_1}$ (bottom). In case of the baseline VAE, we observe similar intra-state and inter-state distances. This implies that samples of different states are encoded close together in the latent space which can raise ambiguities when planning. On the contrary, when using $VAE_{12-ns-L_1}$, we observe that the inter- and intra-state distances approach the values 5 and 0, respectively. These values are imposed with the action term (4) as the minimum distance d_m reaches 2.6. Therefore, even when there exists no direct link between two samples of different states, and thus the action term for the pair is never activated, the VAE is able to encode them such that the desired distances in the latent space are respected.

Similar conclusions also hold in the hard stacking task for which the inter- (in blue) and intra-state (in orange) distances are depicted in Fig. 9. Top row again shows the distances calculated with the baseline model $VAE_{12-hs-b}$, while the ones shown in the bottom are obtained with the action model $VAE_{12-hs-L_1}$. Note that we obtained lower inter-state distance than in case of *ns* because in *hs* the minimum distance d_m reached only 2.3.

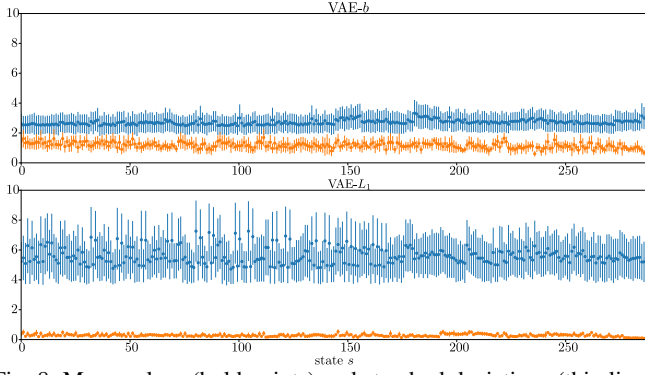


Fig. 8: Mean values (bold points) and standard deviations (thin lines) of inter- (blue) and intra- (orange) state distances for each state calculated using the baseline VAE (top) and the action VAE_{12-ns-L1} model (bottom). The normal stacking task is considered.

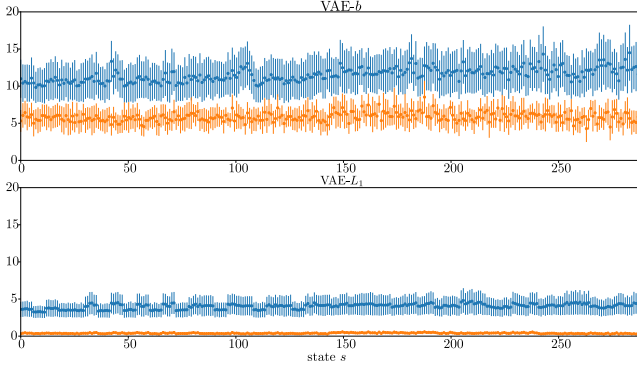


Fig. 9: Mean values (bold points) and standard deviations (thin lines) of inter- (blue) and intra- (orange) state distances for each state calculated using the baseline VAE (top) and the action VAE_{12-hs-L1} model (bottom). The hard stacking task is considered.

Finally, we analyzed the difference between the minimum inter-state distance and the maximum intra-state distance for each state. The higher the value the better separation of states in the latent space since samples of the same state are in this case closer to each other than samples of different states. When the latent states were obtained using the baseline VAE_{12-ns-b}, we observe a non-negative distance for 0/288 states with an average value of ≈ -1.2 . This implies that only weak separation occurs in the latent space for samples of different states. On the other hand, when calculated on points encoded with VAE_{12-ns-L1}, the difference becomes non-negative for 284/288 states and its mean value increases to ≈ 0.55 , thus achieving almost perfect separation. In the hard stacking task, we similarly found that VAE_{12-hs-b} reached an average difference of -5.86 (being non-negative for 0/288 states), while the action model VAE_{12-hs-L1} reduced the average difference to -0.04 (being non-negative for 121/288 states). This result validates the difference in the difficulty between the two versions of the box stacking task and highlights the challenges of visual action planning on the harder stacking task where worse separation of states is achieved. *We conclude that the action term (4) and the dynamic setting of d_m contribute to a better structured latent space \mathcal{Z}_{sys} .*

3) Separability of data samples: To further analyze how the action loss influences the structure of the latent space, we resorted to the concept of *relative contrast*, introduced

in [41] and based on [42]. Given a dataset \mathcal{T} containing ld -dimensional data points, the relative contrast rc of \mathcal{T} with respect to the metric L_p is defined as

$$rc(\mathcal{T}, ld, p) = \frac{D_{\max} - D_{\min}}{D_{\min}} \quad (10)$$

where D_{\max} denotes the distance of the furthest point in the dataset \mathcal{T} from the origin, and similarly, D_{\min} the distance of the closest point in \mathcal{T} to the origin in \mathbb{R}^{ld} . According to [41], the origin can be replaced by any other chosen point. In our case, we calculated rc of the latent training dataset \mathcal{T}_z using VAEs with different latent dimensions ld . The obtained rc values were used to evaluate significance of distances among points in the latent space \mathcal{Z} , where a lower rc implies diminishing contrast in distances.

The authors of [42] show that, under broad assumptions, rc converges to 0 when ld approaches infinity, as in this case the distance from any point to its nearest neighbor becomes identical to the distance to its furthest neighbor. This result highlights the importance of the choice of the latent dimension ld . On one hand, it needs to be large enough to encode all the relevant features for the task, while on the other hand, an ld too large weakens the significance of distances in which case calculating nearest neighbours becomes increasingly difficult.

In our case, measuring rc on the full dataset can be misleading since the latent no-action pairs are encoded closeby because of the action term (4). This would lead to a deceptively small D_{\min} and therefore to a higher rc than warranted. To get a reliable estimate of rc given \mathcal{T}_z , we therefore chose to measure it in the following way. We split the latent training dataset \mathcal{T}_z into datasets \mathcal{T}_z^1 and \mathcal{T}_z^2 containing the first and the consecutive states of all the training tuples in \mathcal{T}_z , respectively. We then measured D_{\min} and D_{\max} with respect to each state in \mathcal{T}_z^1 and \mathcal{T}_z^2 separately. More precisely, we considered each latent state $z_i \in \mathcal{T}_z^1$ as the origin, and calculated D_{\min} (and D_{\max}) within $\mathcal{T}_z^1 \setminus \{z_i\}$. We repeated the same process for all $z_i \in \mathcal{T}_z^2$. Finally, we used the average of the obtained D_{\min} and D_{\max} values in the computation of rc as in (10).

Table III reports the relative contrast of \mathcal{T}_z for both versions of the stacking task. The distances were calculated using baseline and L_1 action VAEs when varying the dimension of the latent space ld . We observe that VAE_{ld-L1} achieved a higher rc than the baseline VAE_{ld-b}. This is because the action loss (4) encourages no-action pairs to be encoded closeby, hence minimizing D_{\min} , and action pairs to be encoded at least d_m apart, hence encouraging D_{\max} to be at least d_m . From the same reason, rc decreases with increasing ld for baseline VAEs, while it is rather constant for the action models VAE_{ld-L1}. Moreover, we obtained higher rc values for ns than hs which once more highlights the differences in difficulty between the two versions of the stacking task. *We thus conclude that the action term and the dynamic setting of d_m improve the relative contrast.*

4) VAE compared to AE: VAE framework is only one of the possible models for the MM. We justify this modeling choice by comparing it with the AE framework. Similarly as VAE, an AE model consists of an encoder and a decoder network which are jointly trained to minimize the difference

ld	normal stacking (ns)		hard stacking (hs)	
	VAE_{ld-b}	VAE_{ld-L_1}	VAE_{ld-b}	VAE_{ld-L_1}
4	73.9	159.7 ± 23.9	29.2	93.8 ± 10.1
6	19.4	59.8 ± 4.1	11.7	39.2 ± 2.3
8	11.7	45.6 ± 1.6	8.3	24.1 ± 1.8
12	5.7	46.0 ± 7.0	4.8	20.6 ± 1.6
16	4.4	40.4 ± 8.1	3.9	21.6 ± 2.3
32	3.7	46.0 ± 4.3	3.7	29.9 ± 3.9
64	3.4	41.8 ± 3.0	3.7	21.9 ± 2.6

Table III: Evaluation of the relative contrast rc on \mathcal{T}_z obtained with the baseline VAE and the action VAEs. Results for the normal (left) and hard (right) stacking tasks are reported.

between the original input and its decoded output. In contrast to VAEs, the two networks in AEs do not model a probability distribution. While there exists extensions of AEs with generative capability [43] [44], we used the basic formulation where the training objective is to minimize the Mean Squared Error (MSE) between the input and decoded output. We refer to it as AE- b . Analogously to VAEs in Sec. V, the original AE loss was augmented with the action loss (4) weighted by the hyperparameter γ . We refer to the latter model as AE- L_p where L_p refers only to the metric used in (4) and not in the calculation of the MSE.

We modelled the AE encoder and decoder networks using the same ResNet [40] architecture as in case of VAEs. We set $ld = 12$, $\gamma = 1000$ and increased the minimum distance d_m dynamically every fifth epoch starting from 0 using $\Delta d_m = 1$, as described in Sec. V. The LSR was built using the same $\tau_{\min} = 0$ and $\tau_{\max} = 3$ (Algorithm 2).

Table IV shows the LSR performance on the hard stacking task when MM is modelled as AE (top two rows) and as VAE (bottom row) using metric L_1 . Not only we observe a superior performance of VAE compared to the AE but again demonstrate the effectiveness of the action term (4) as it increases the AE performance from 0.12% to 36.36%. The same conclusion holds for the normal stacking task as reported in Appendix-1. *This comparison shows that the probabilistic modeling adopted by VAEs results in a latent space that is more adequate for visual action planning with respect to AEs.*

Model	% All	% Any	% Trans.
AE- b +LSR- L_1	0.1 ± 0.03	0.12 ± 0.04	31.79 ± 2.58
AE- L_1 +LSR- L_1	28.93 ± 7.79	36.36 ± 8.42	84.42 ± 3.24
VAE- L_1 +LSR- L_1	90.9 ± 3.5	92.1 ± 2.9	95.8 ± 1.3

Table IV: Comparison of the LSR performance when modelling MM with the AE (top two rows) and VAE (bottom row) frameworks on the hard stacking task. Best results in bold.

5) Dataset size: The size of the training dataset is crucial for many learning based approaches where the collection of training data can be very costly. We therefore investigated the effect of the size of the training data on the performance of the LSR on the hard stacking task. We evaluated two $VAE_{12-hs-L_1}$ models where the first one was trained on a dataset \mathcal{T}_I of size $|\mathcal{T}_I| = 2500$, and the second one using $|\mathcal{T}_I| = 5000$. In the former case, the LSR performance measured by the partial scoring reached $92.1 \pm 2.9\%$, while in the latter case it reached $96.6 \pm 1.5\%$. Hence, having twice

the amount of data leads to an $\approx 4.5\%$ improvement in the LSR performance.

Note that in both cases the size of the datasets is much smaller compared to the number of all possible combinations of states of the system. In particular, the latter is given by $(n+1)n/2$ for a system with n different states, which results in 41616 possible combinations as $n = 288$ in the stacking task. This shows the strength of our approach in terms of data efficiency: we achieve a satisfactory performance of $\approx 92\%$ (on the harder version) using only 2500/41616 possible pairs, which corresponds to 6% of all possible state pairs.

This experiments demonstrates both the data-efficiency of the proposed approach as well as benefits of enlarging the size of the training dataset, and consequently the covered regions.

6) Latent space dimension: The problem of choosing a suitable latent space dimension has not received much attention in the literature. Even though the action term alleviates the problem of indistinguishable distances in higher dimensions by increasing the relative contrast, it is still important to choose a latent dimension large enough so that the relevant features can be encoded.

In Table V we report the performance of the LSR on both normal and hard stacking tasks using VAE models with various latent dimensions. The LSR performance is measured with the partial scoring. The results demonstrate an evident drop in the performance when the latent dimension is too small, such as $ld = 4$. As ld increases, we observe gradual improvements in the performance where a satisfactory level is achieved using $ld \geq 6$ for ns , and $ld \geq 12$ for hs . Therefore, hs requires more dimensions in order to capture all the relevant and necessary features. *This result not only demonstrates the complexity of each task version but also justifies the choice $ld = 12$ in the rest of the box stacking experiments.*

ld	ns [%]	hs [%]
4	7.9 ± 2.2	8.8 ± 7.9
6	99.96 ± 0.08	56.2 ± 23.1
8	99.96 ± 0.08	62.7 ± 18.7
12	100.0 ± 0.0	92.1 ± 2.9
16	100.0 ± 0.0	95.9 ± 1.4
32	97.5 ± 4.33	96.4 ± 0.4
64	99.8 ± 0.5	95.3 ± 0.9

Table V: Comparison of the LSR performance when using VAEs with different latent dimensions for the normal (left) and hard (right) box stacking tasks.

C. LSR Analysis

In this section, we analyzed the performance of the LSR with respect to its parameters and the choice of the clustering algorithm as stated in point 2) in Sec. VIII-A. Firstly, we analyzed the LSR performance depending on whether or not the action term was included in the VAE loss function. Secondly, we investigated the influence of the upper bound on the number of connected components c_{\max} used in (8). Thirdly, we performed an extensive comparison of the LSR algorithm using different clustering algorithms in Phase 2 of Algorithm 1. Finally, we analyzed the covered regions determined by the LSR.

1) LSR performance: We analyzed the performance of the LSR for both tasks and investigated how it is affected by the action term (4). We considered the baseline models VAE_{12-b} and the action VAE_{12-L₁} trained with the action term (4) using metric L_1 , and evaluated the LSR performance when building the LSR using metric L_1 . Table VI reports the full scoring on the normal (top part) and hard (bottom part) box stacking tasks. The results show deteriorated LSR performance when using baselines VAE_{12-b} compared to the action VAEs regardless the version of the task. This indicates that VAEs- b are not able to separate states in \mathcal{Z}_{sys} . We again conclude that the action term (4) needs to be included in the VAE loss function (6) in order to obtain distinct covered regions \mathcal{Z}_{sys}^i . In addition, the results confirm the different level of difficulty of the two tasks as indicated by the drop in the LSR performance on hs compared to ns using the action VAE- L_1 .

Similarly to our earlier work [9], we also analyzed the influence of the choice of the metric on the LSR performance which confirmed a superior performance of L_1 compared to L_2 and L_∞ . All the results are provided in the Appendix-2.

In summary, this experiment validates the effectiveness of the LSR for performing normal and hard box stacking as well as confirms the need to integrate the action term in the VAE loss function.

Task	Model	% All	% Any	% Trans.
ns	VAE- b + LSR- L_1	2.5 ± 0.5	4.1 ± 1.0	59.7 ± 4.9
	VAE- L_1 + LSR- L_1	100.0 ± 0	100.0 ± 0	100.0 ± 0
hs	VAE- b + LSR- L_1	0.2 ± 0.1	0.2 ± 0.1	38.0 ± 2.0
	VAE- L_1 + LSR- L_1	90.9 ± 3.5	92.1 ± 2.9	95.8 ± 1.3

Table VI: LSR performance for the normal (top part) and hard (bottom part) box stacking tasks using the action VAE- L_1 and baseline VAE- b . Best results in bold.

2) Influence of the maximum number of connected components: The optimisation method described in Sec. VI-B requires setting an upper bound on the number of graph-connected components c_{max} of the LSR. Table VII shows how different upper bounds influence the LSR performance on both normal and hard stacking tasks. We evaluated LSR on partial scoring using VAE_{12-ns-L₁} and VAE_{12-hs-L₁}.

c_{max}	ns [%]	hs [%]
1	100.0 ± 0.0	65.3 ± 24.6
5	99.5 ± 0.4	88.6 ± 5.4
10	99.0 ± 0.3	91.5 ± 3.8
20	97.5 ± 0.5	92.1 ± 2.9
50	91.3 ± 1.1	88.2 ± 2.0
100	80.0 ± 1.4	77.9 ± 2.1

Table VII: LSR performance measured as partial scoring on normal ns (first column) and hard hs (second column) stacking tasks for different c_{max} . Best results shown in bold.

We observe that the results are rather robust with respect to the c_{max} value. For both task versions, the performance drops for a very high c_{max} , such as $c_{max} = 100$, while in the hard stacking task we additionally observe a drop for a very low c_{max} , such as $c_{max} = 1$. This behavior can be explained by the fact that the lower the c_{max} the more the system is sensitive to outliers, while the higher the c_{max} the greater the possibility that the obtained graph is disconnected which potentially

compromises its planning capabilities. For example, in the hard stacking task, outliers arise from different lightning conditions. In contrast, no outliers exists in the normal stacking task which is why a single connected component is sufficient for the LSR to perform perfectly. For all further evaluation we set $c_{max} = 1$ and $c_{max} = 20$ for the normal and hard box stacking tasks, respectively.

This experiment validates the robustness of the approach with respect to the parameter c_{max} as well as justifies the choices $c_{max} = 1$ and $c_{max} = 20$ for ns and hs , respectively, in the rest of experiments.

3) Comparing different clustering methods for Phase 2:

We compared different clustering methods used in Phase 2 in Algorithm 1 on the normal and hard stacking tasks. We also showcase the effect of the outer optimisation loop described in Algorithm 2 with all the clustering methods. In the following, we first summarize the considered clustering algorithms and list their hyperparameters.

Epsilon clustering: the epsilon-clustering algorithm is used in Phase 2 in our earlier work [9] and is functionally identical to the DBSCAN [45] algorithm. Its performance heavily depends on the parameter ε defining the radius of the ε -neighborhood of every point, and deteriorates when clusters have different densities [46].

Mean-shift: centroid-based algorithm [47] adopting a moving window approach to identify high density regions. At each iteration, the centroid candidates associated to the windows are updated to be the mean of the points within the considered region. The size of the window has a significant influence on the performance and is determined by the bandwidth of the RBF kernel in the chosen implementation [48].

OPTICS: improved version of DBSCAN [45] introduced by [49]. The main difference to DBSCAN is that OPTICS builds hierarchical reachability-plot dendrogram, the slope of which identifies the clusters with different densities. The parameter $\Xi \in [0, 1]$ is used to tune the slope and, therefore, Ξ heavily affects the outcome of the algorithm but its influence is not easy to understand intuitively, as discussed in [50].

Linkage: hierarchical, agglomerative clustering algorithm [51] that merges individual points in a step by step fashion until only a single cluster remains. The points are merged using different dissimilarity functions that evaluate the dissimilarity between two clusters, such as *single*, *complete* and *average*. The *single* dissimilarity function considers the minimum distance between any pair of points belonging to two distinct clusters, while the *complete* dissimilarity function considers the maximum distance. The *average*-linkage clustering, also called UPGMA [31], defines the dissimilarity function as the unweighted average of the distances of all points belonging to two distinct clusters. As discussed in Sec. VI-A, the data-structure returned by the linkage algorithm is a stepwise dendrogram [8] which is used to extract different disjoint clusters depending on the chosen level of hierarchy. The latter is defined by a clustering threshold τ that determines the vertical cut through the dendrogram and consequently influences the performance of the algorithm. Note that we choose to use the average-linkage to build the LSR.

HDBSCAN: an agglomerative clustering algorithm with an optimized dendrogram cut [52]. As opposed to performing a single global cut through the dendrogram such as in DBSCAN [45], the branches of the dendrogram are optimised for non-overlapping clusters using a notion of “cluster stability” based on their longevity. HDBSCAN automatically identifies clusters with different densities and requires specifying only the minimum cluster size prior to the training.

Optimization criterion: The performance of the listed clustering methods (except for HDBSCAN) depends on a single input scalar parameter that is hard to tune. However, as described in Sec. VI-B, we are able to optimise it by maximizing the number of edges in all connected components of the LSR while imposing an upper bound on the number of components (see Algorithm 2). To validate that this optimization criterion improves the LSR performance, we compared it with the best result found by performing a grid search over the respective clustering parameter. Note that such grid search is only possible in this problem setting as the ground truth can be retrieved from the trained classifiers but it is not generally applicable.

In Table VIII we report the LSR performance evaluated with partial scoring on the hard stacking task using $\text{VAE}_{12}\text{-hs-}L_1$ and the introduced clustering algorithms. The left column corresponds to the best performance of the clustering algorithms for which the input parameters were found by performing a grid search, while the right column corresponds to the performance of the clustering algorithms where the input parameter was determined using our automatic optimization.

Firstly, the results show that average-linkage, used for our LSR in Sec. VI-A, together with our automatic input parameter optimization outperforms the other alternatives. The results of the grid search show that the automatic criteria for identifying different cluster densities, adopted by OPTICS and HDBSCAN, do not effectively retrieve the underlying covered regions. Meanshift performs better but its approximation of spherical clusters does not lead to the optimal solution. Similar performance to Meanshift is obtained with single- and complete-linkage algorithms showing that the respective distance functions are not either suited for identifying covered regions. The same applies for the epsilon clustering.

Concerning the optimization results, they highlight the effectiveness of the optimization procedure in Algorithm 2 as they are comparable to the ones obtained with the grid search for all clustering methods. Note that grid search leads to a slightly lower performance than the optimization for meanshift, complete-linkage and UPGMA agglomerative clusterings. In these cases, the grid is not fine enough which points out the difficulty of tuning the respective parameters.

For the normal task, all the methods except for OPTICS reached average performance higher than 99.7% when applying the optimization, while OPTICS reached $\approx 91\%$. These results were obtained using $\text{VAE}_{12}\text{-ns-}L_1$ and further discussed in the Appendix-3.

This investigation demonstrates the effectiveness of our proposed optimization of the clustering threshold τ and shows that the average-linkage clustering algorithm leads to the best LSR performance for the box stacking task.

Clust. method	Grid Search [%]	Optimization [%]
Epsilon [9]	83.5 ± 4.8	65.8 ± 12.2
Meanshift	78.2 ± 3.3	80.2 ± 5.9
OPTICS	44.3 ± 8.7	40.8 ± 6.1
HDBSCAN	16.1 ± 5.7	-
Single-linkage	79.3 ± 8.8	65.8 ± 12.2
Complete-linkage	79.1 ± 6.4	81.4 ± 4.8
Average-linkage	91.1 ± 2.5	92.1 ± 2.9

Table VIII: Comparison of the LSR performance for different clustering algorithms for the hard box stacking task. Partial scoring is reported when applying grid search (left column) and when using the optimization in Algorithm 2 (right column). Best results in bold.

4) Covered regions using LSR: In order to show that the LSR captures the structure of the system, we used it to determine if various novel observations are recognized as covered or not. We first checked if observations corresponding to true underlying states of the system, that have not been seen during training, are properly recognized as covered. We then checked if observations taken from standard datasets, such as CIFAR10 [53] and 3D Shapes [54], are marked as uncovered since they correspond to out-of-distribution observations, sampled from a distribution different than the one of the training observations. The covered regions \mathcal{Z}_{sys}^i were computed using the epsilon approximation in (7).

Table IX reports the results of the classification of covered states for both normal (top block) and hard (bottom block) box stacking tasks when additionally varying the training dataset size $|\mathcal{T}_I|$. The results were produced using $\text{VAE}_{12}\text{-ns-}L_1$ and $\text{VAE}_{12}\text{-hs-}L_1$ trained with 5 different random seeds. We considered 5000 novel observations that correspond to covered states of both the normal and hard box stacking tasks, and report the percentage of those classified as covered. The higher this percentage the better the classification.

The table shows that the LSR almost perfectly recognized all the covered states for the normal task with the average recognition equal to 99.5% when $|\mathcal{T}_I| = 2500$. This percentage then increased to 99.7% when more training data samples were used, *i.e.*, when $|\mathcal{T}_I| = 5000$. For the hard stacking task, LSR properly recognized on average 4694/5000 samples (93.9%) when the model was trained with 2500 pairs and 4871/5000 samples (97.4%) when trained with 5000 pairs. This is motivated by the fact that a higher number of training samples better covers the latent space.

Regarding the out-of-distribution observations, we sampled 5000 images from each of the 3D Shapes and CIFAR-10 datasets, and evaluated the percentage of those recognized as covered. In this case, the lower the percentage the better the classification. As shown in Table IX, almost all the samples in both datasets were correctly recognized as not covered with all the models. In particular, the classification with CIFAR-10 only failed with an average percentage lower than 0.03% in all the cases. Regarding 3D Shapes, we obtained a perfect recognition for all the cases, except for the normal stacking model with $|\mathcal{T}_I| = 5000$ for which a low failure percentage is obtained (0.1%).

We conclude that LSR successfully captures the global structure of the system as it correctly classifies the observations

representing the possible states of the system as covered, and out-of-distribution observations as not covered.

	$ \mathcal{T}_I $	Boxes [%]	CIFAR-10 [%]	3D Sh. [%]
ns	2500	99.5 ± 0.3	0.008 ± 0.011	0 ± 0
	5000	99.7 ± 0.2	0.008 ± 0.011	0.1 ± 0.2
hs	2500	93.9 ± 0.7	0.028 ± 0.044	0 ± 0
	5000	97.4 ± 0.5	0.008 ± 0.011	0 ± 0

Table IX: Classification of covered states for the normal and hard box stacking models when considering as inputs novel boxes images (left column) as well as images from CIFAR-10 and 3D Shapes datasets (middle and right columns). We report the results obtained with different training dataset sizes $|\mathcal{T}_I|$.

D. APM Analysis

We evaluated the accuracy of action predictions obtained by APN- L_1 on an unseen test set consisting of 1611 and 1590 action pairs for the normal and hard stacking task, respectively. As the predicted actions can be binary classified as either true or false, we calculated the percentage of the correct proposals for picking and releasing, as well as the percentage of pairs where both pick and release proposals were correct. For both task versions, all the models performed with 99% or higher accuracy evaluated on 5 different random seeds determining the training and validation sets². This is because the box stacking task results in an 18-class classification problem for action prediction which is simple enough to be learned from any of the VAEs.

IX. FOLDING EXPERIMENTS

In this section, we validated the proposed approach on a real world experiment involving manipulation of deformable objects, namely folding a T-shirt. As opposed to the box stacking task, the true underlying states are in this case unknown and it is therefore not possible to define an automatic verification of the correctness of a given visual action plan.

The folding task setup is depicted in Fig. 12 (middle). We used a Baxter robot equipped with a Primesense RGB-D camera mounted on its torso to fold a T-shirt in different ways. The execution videos of all the performed experiments and respective visual action plans can be found on the project website¹. A summary of the experiments can also be found in the accompanying video. For this task, we collected a dataset \mathcal{T}_I containing 1283 training tuples. Each tuple consists of two images of size $256 \times 256 \times 3$, and action specific information u defined as $u = (p, r, h)$ where $p = (p_r, p_c)$ are the picking coordinates, $r = (r_r, r_c)$ the releasing coordinates and h picking height. An example of an action and a no-action pair is shown in Fig. 4. The values $p_r, p_c, r_r, r_c \in \{0, \dots, 255\}$ correspond to image coordinates, while $h \in \{0, 1\}$ is either the height of the table or a value measured from the RGB-D camera to pick up only the top layer of the shirt. Note that the latter is a challenging task in its own [55] and leads to decreased performance when it is necessary to perform it, as shown in Sec. IX-E2. The dataset \mathcal{T}_I was collected by manually selecting pick and release points on images showing a given T-shirt configuration, and recording the corresponding action and

following configuration. No-action pairs, representing $\approx 37\%$ of training tuples in \mathcal{T}_I , were generated by slightly perturbing the cloth appearance.

A. Experiment Objectives and Implementation Details

The experiments on the real robot are designed to answer the following questions:

- 1) **MM** Does the action loss term (4) improve the structure of the latent space for the folding task?
- 2) **LSR** How good is the approximation of the covered regions provided by the LSR for a real world dataset?
- 3) **APM** How does the APN perform in comparison to alternative implementations of the APM?
- 4) **System** How does the real system perform and how does it compare to our earlier work [9]? What is the performance on a folding that involves picking the top layer of the shirt?

Similarly to Sec. VIII-A, we denote by VAE_{ld-f-d} a VAE with ld -dimensional latent space, where f stands for the folding task and d indicates whether or not the model was trained with the action loss (4). We use $d = b$ for the *baseline* VAEs which were trained with the original training objective (5). We use $d = L_p$ for the *action* VAEs trained with the objective (6) containing the action term (4) using metric L_p for $p \in \{1, 2, \infty\}$. We model VAEs with the same ResNet architecture and same hyperparameters β, γ and d_m as in the box stacking task introduced in Sec. VIII but increased the latent space dimension to $ld = 16$. We refer the reader to the code repository² for the exact implementation details.

For the LSR, we keep the same notation as in Sec. VIII-C, where $\text{LSR}-L_p$ denotes a graph obtained by using metric L_p in Algorithm 1. We set the upper bound c_{\max} on the maximum number of graph-connected components in (8) to 5, and the search interval boundaries τ_{\min} and τ_{\max} in Algorithm 2 to 0 and 3.5, respectively.

The performance of the APMs and the evaluation of the system is based on the VAE_{16-f-L_1} realization of the MM. We therefore performed the experiments using APN_{16-f-L_1} which was trained on latent action pairs $\bar{\mathcal{T}}_z$ extracted by the latent mapping ξ of VAE_{16-f-L_1} . We trained 5 models for 500 epochs using different random seeds as in case of VAEs, and used 15% of the training dataset as a validation split to extract the best performing model for the evaluation.

We compared the performance of our system S-OUR consisting of VAE_{16-f-L_1} , $\text{LSR}-L_1$ and APN_{16-f-L_1} with the systems S- L_1 , S- L_2 and S- L_∞ introduced in [9] on the same five folding tasks. The start configuration is the fully unfolded shirt shown in Fig. 10 on the left, while the goal configurations are shown on the right. The latter are of increasing complexity requiring a minimum of 2, 2, 3, 3, and 4 folding steps for folds 1-5, respectively.

Each fold was repeated five times and scored in the same way as in [9]. In particular, we scored the *system performance* where a folding was considered successful if the system was able to fold the T-shirt into the desired goal configuration. As the state space of the T-shirt is high-dimensional, there exists no objective measure that would evaluate the success of the

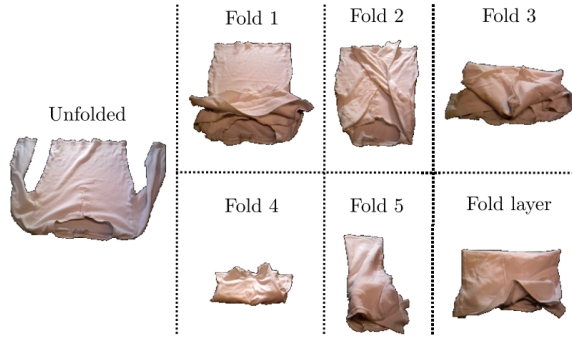


Fig. 10: Unfolded start state (right) followed by five different goal configurations for the folding task [9]. The lower right configuration requires to pick a layer on top of the T-shirt.

fold automatically. Therefore, the evaluation of the full folding procedure was done by a human¹. We additionally evaluated the percentage of successful *transitions of the system*. A transition was considered successful if the respective folding step was executed correctly. Lastly, we evaluated the quality of the generated visual plans P_I and the generated action plans P_u . We considered a visual (action) plan successful if all the intermediate states (actions) were correct. This evaluation was done for a given fold on the very first generated visual action plan by a human.

Even for a correctly generated visual action plan, the open loop execution is not robust enough for a real robot system. We therefore added a re-planning step after each action completion as shown in Fig. 12. This accounts for potential execution uncertainties, for example, inaccuracies in grasping or in the positioning phases of pick-and-place operations which lead to observations different from the ones planned in P_I . Note that after each action execution, the current observation of the cloth is considered as a new start observation, and a new visual action plan is produced until the goal observation is reached or the task is terminated. Such re-planning setup was used for all folding experiments. As the goal configuration does not allude to how the sleeves should be folded, the LSR suggests multiple latent plans. A subset of the corresponding visual action plans is shown on the left of Fig. 12. If multiple plans are generated, a human operator selects one to execute. After the first execution, the ambiguity arising from the sleeve folding is removed, and the re-planning generates a single plan, shown in the right.

To deal with the sparse nature of the collected dataset, if no path is found from the start to the goal node, the planning is repeated using the closest nodes to the current start and/or goal nodes in the latent space. This procedure is repeated until a path is found.

B. MM Analysis

Analogously to the box stacking task in Sec. VIII-B, we answered question 1) by analyzing the relative contrast as well as by evaluating the separation of action and no-action pairs during the training.

1) Separability of data samples: Table X shows the relative contrast rc of \mathcal{T}_z produced by the baseline models VAE_{16-f-b} (left) and action models VAE_{16-f-L_1} (right)

when varying the latent space dimension ld . For the action models (right) we report the mean and standard deviation of rc computed over 5 random seeds. We observe that the action term (4) significantly increases the relative contrast also for the folding task, but clearly drops for higher latent dimensions which is consistent with the results obtained for the box stacking task in Sec. VIII-B3.

ld	VAE_{ld-f-b}	VAE_{ld-f-L_1}
4	24.2	37.7 ± 4.3
6	13.7	26.1 ± 2.7
8	10.2	22.3 ± 2.2
12	7.2	15.8 ± 3.2
16	5.8	12.1 ± 1.2
32	4.5	8.2 ± 0.8
64	3.7	8.1 ± 0.8

Table X: Relative contrast evaluation comparing baseline (left column) and action VAEs (right column) when varying the latent space dimension ld .

2) Influence of dynamic d_m : Next, we investigated the influence of the dynamic increase of d_m in the action term (4) on the structure of the latent space. Fig. 11 shows the histogram of action (in blue) and no-action (in green) pair distances calculated at different epochs during training using VAE_{16-f-b} (top row) and VAE_{16-f-L_1} (bottom row). We observe that the separation was complete in case of action VAEs but was not achieved with the baseline VAEs. To precisely quantify the amount of overlap between action and no-action pairs, we calculated the difference between the minimum action-pair distance and maximum no-action pair distance on the training dataset. Therefore, a positive value implies that action pairs were successfully separated from the no-action pairs. For VAE_{16-f-b} (top row), the difference evaluated to -31.8 , -19.2 , and -19.4 for epoch 1, 100, and 500, respectively, while it was improved to -6.3 , -1.6 , and 1.5 in case of the action VAE_{16-f-L_1} (bottom row). This shows that the dynamic selection of d_m successfully separates the actions and no-action pairs also for the folding task.

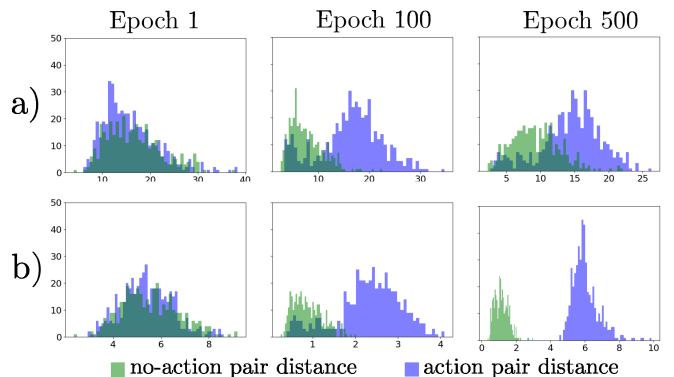


Fig. 11: Histograms of the action (in blue) and no-action (in green) pair distances at different training epochs (epoch 1, 100 and 500 from the left, respectively) for the folding task. The figure shows the results obtained with the baseline model (top row, a)) and with the action model (bottom row, b)).

Method	X Pick	Y Pick	X Release	Y Release	Height	Total
e-APN [9]	144.1 \pm 52.2	52.8 \pm 18.3	317.2 \pm 143.3	159.9 \pm 17.4	0.0 \pm 0.0	674.0 \pm 147.6
C-APN	498.0 \pm 63.8	47.4 \pm 7.7	818.8 \pm 121.9	226.5 \pm 92.5	0.0 \pm 0.0	1590.8 \pm 155.0
R-APN	697.2 \pm 345.1	246.2 \pm 174.9	792.4 \pm 388.8	268.9 \pm 157.0	0.0 \pm 0.0	2004.6 \pm 908.2
AAB	113.0	22.4	201.4	194.7	0.0	531.5
APN (Ours)	82.6 \pm 22.9	29.3 \pm 2.2	270.6 \pm 158.2	71.8 \pm 15.0	0.0 \pm 0.0	454.3 \pm 153.8

Table XI: Comparison of MSE achieved with different realizations of the Action Proposal Modules. Best results in bold.

C. LSR Analysis

Similarly to the box stacking case, we exploited the LSR to investigate the covered regions of the latent space \mathcal{Z} , thus answering question 2) listed in Sec. IX-A. Note that in Sec. IX-E, the LSR was also employed to perform the folding task with the real robotic system.

1) Covered regions using LSR: We used VAE₁₆- f - L_1 model and reproduced the experiment from Sec. VIII-C4, where we measured the accuracy of various novel observations being recognized as covered. We input 224 novel observations that correspond to possible states of the system and were not used during training, as well as 5000 images from each of the 3D Shapes and CIFAR-10 datasets which represent the out-of-distribution samples that are not resembling the training data. We observe that the LSR achieved good recognition performance even in the folding task. More precisely, on average 213/224 samples representing true states of the system were correctly recognized as covered, resulting in $95 \pm 2.4\%$ accuracy averaged over the 5 different random seeds. For 3D Shapes dataset, 0/5000 samples were recognized as covered, while only 20/5000 samples from the CIFAR-10 dataset were on average wrongly recognized as covered.

This analysis confirms the effectiveness of the LSR in capturing the covered regions of the latent space. It also shows the greater complexity of learning the latent mapping on real world observations, representing states of deformable objects, than on the simulated observations.

D. APM Comparison

In this section we validated the choice of the APM by comparing it to several possible alternatives.

The Action Proposal Network, described in Sec. VII, is built upon the one introduced in [9] to which we added dropout regularization layers. The APN receives as inputs latent action pairs contained in a latent plan found by the LSR, and outputs the predicted action specifics. We refer to the *earlier* version in [9] as *e-APN* and to the current version APN₁₆- f - L_1 as *APN*. We compared the performance of APN to e-APN as well as several alternatives introduced below.

Action Averaging Baseline (AAB) Firstly, we investigated whether the action predictions can be retrieved directly from the LSR instead of a separate module. The basic idea is to use the latent action pairs in the training dataset to calculate the average action specifics associated with each edge in the LSR. Let $\mathcal{E}_{sys}^{ij} = \{(z_1, z_2) \in \mathcal{E} | z_1 \in \mathcal{Z}_{sys}^i, z_2 \in \mathcal{Z}_{sys}^j\}$ be the set of edges from the reference graph \mathcal{E} connecting covered regions \mathcal{Z}_{sys}^i and \mathcal{Z}_{sys}^j (Algorithm 1). We parameterized each edge

$e_{LSR}^{ij} = (z_{LSR}^i, z_{LSR}^j) \in \mathcal{E}_{LSR}$ with the action u_{LSR}^{ij} obtained by averaging actions corresponding to the edges in \mathcal{E}_{sys}^{ij}

$$u_{LSR}^{ij} = \frac{1}{|\mathcal{E}_{sys}^{ij}|} \sum_{(z_1, z_2) \in \mathcal{E}_{sys}^{ij}} u^{z_1 z_2} \quad (11)$$

where $u^{z_1 z_2}$ is the action specification associated with the action pair (z_1, z_2) in the training dataset \mathcal{T}_z . The parametrization (11) yields the action plan associated with a path P_z .

Secondly, we investigated how the use of the latent encodings as inputs to the APM influences the LSR performance. We compared APN-d with two distinct versions of APMs that use images as inputs.

C-APN is a neural network that uses a convolutional encoder followed by the APN. The encoder in C-APN was trained using only MSE loss. During the inference, the observations given to C-APN as input are obtained by decoding the latent plan found by the LSR with the observation generator ω .

R-APN is an extension of C-APN that instead of a convolutional encoder uses a ResNet encoder identical to the VAE encoder.

Detailed architectures of all the models can be found in our code repository². The training details for APN and APN-d are described in Sec. IX-A. For C-APN-d and R-APN-d, we similarly trained 5 models using different random seeds but on a training dataset $\overline{\mathcal{T}}_I$ obtained by decoding $\overline{\mathcal{T}}_z$ with the observation generator ω of VAE₁₆- f - L_1 . This is because the visual plans, given to C-APN-d and R-APN-d, are produced by decoding the latent plans with ω . Moreover, C-APN-d and R-APN-d were instead trained for 1000 epochs to ensure the convergence of the initialized encoders. Note that we can only obtain one AAB model for a chosen VAE as AAB is defined by the LSR.

We evaluated the performance of all the models on a holdout dataset consisting of 41 action pairs. Given a holdout action pair, we calculated the mean squared error (MSE) between the predicted and the ground truth action specifics. We report the mean and standard deviation of the obtained MSE calculated across the 5 random seeds (except for AAB). The results are shown in Table XI where we separately report the error obtained on picking and releasing as well as the total model error. Firstly, we observe that the added regularization layer positively affects the result as APN achieved lower error than our earlier version e-APN [9]. Secondly, APN significantly outperformed both C-APN and R-APN. Using the latent encodings as inputs also significantly decreases the size of the models and reduces the computational power needed for their training. Lastly, our APN also on average outperformed AAB with respect to the total model error. Although the enhancement compared to the AAB was not

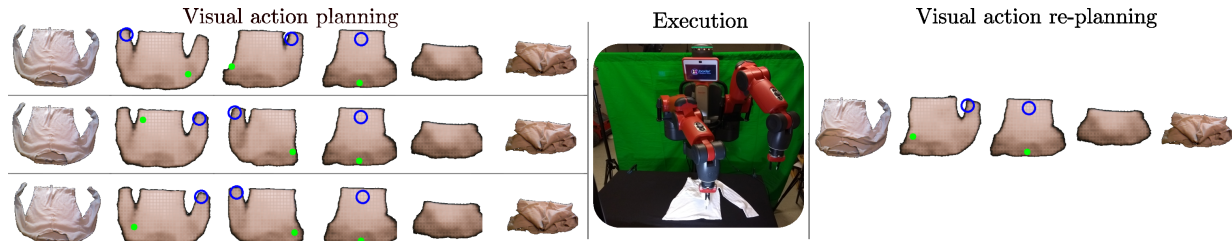


Fig. 12: Execution of the folding task with re-planning. On the left, a set of initial visual action plans reaching the goal state is proposed. After the first execution, only one viable visual action plan remains.

as significant as for the other models, APN is beneficial since it is less prone to averaging errors obtained from the LSR and can be easily adapted to any realization of action specifics. Moreover, a neural network realization of the APM potentially allows more accurate modeling of more complex action specifics. *In summary, using a separate neural network to predict action specifics from latent representations leads to a lower prediction error and can be easily adapted to different types of actions.*

E. System Analysis

We benchmarked our method against our earlier method in [9] on the same T-shirt folding task, and additionally measured the performance on a more challenging fold involving picking a layer of the cloth on top of another layer.

1) Folding performance and comparison with [9]: We performed each fold five times per configuration using the goal configuration shown in Fig. 10 and framework S-OUR, consisting of $\text{VAE}_{16}-f-L_1$, $\text{LSR}-L_1$ and $\text{APN}_{16}-f-L_1$, and compared the performance with the results from our earlier work [9] obtained using $S-L_1$, $S-L_2$ and $S-L_\infty$.

The results are shown in Table XII, while, as previously mentioned, all execution videos, including the respective visual action plans, are available on the website¹. We report the total system success rate with re-planning, the percentage of correct single transitions, and the percentage of successful visual plans and action plans from start to goal. We observe that S-OUR outperformed the systems from [9] with a notable 96% system performance, only missing a single folding step which results in a transition performance of 99%. As for $S-L_1$, S-OUR also achieved optimal performance when scoring the initial visual plans P_I and the initial action plans P_u . *We thus conclude that the improved MM, LSR and APM modules together contribute to a significant better system than in [9].*

2) Folding with multiple layers: As the previous folds resulted in nearly perfect performance of our system, we challenged it with an additional much harder fold that requires to pick the top layer of the garment. The fold, shown in Fig. 10 bottom right, was repeated 10 times. An example of the obtained visual action plan is shown in Fig. 13 and the final results are reported in Table XII (bottom row).

We can see that the system had no trouble planning the folding but failed to pick up the top layer of the T-shirt in half of the cases. This is due to the imprecision of the Baxter and the difficulty of picking up layered clothing. The generated

Method	Syst.	Trans.	P_I	P_u
Fold 1 to 5 - comparison to [9]				
S-OUR	96%	99%	100%	100%
$S-L_1$ [9]	80%	90%	100%	100%
$S-L_2$ [9]	40%	77%	60%	60%
$S-L_\infty$ [9]	24%	44%	56%	36%
Fold layer				
S-OUR	50%	83%	100%	100%

Table XII: Results (best in bold) for executing visual action plans on 5 folding tasks (each repeated 5 times) shown in the top. The bottom row shows the results on the fold requiring to pick the top layer of the garment (repeated 10 times).

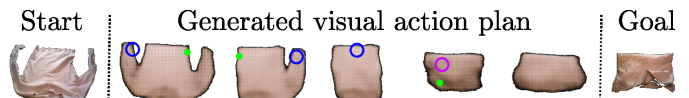


Fig. 13: Visual action plan for the fold requiring to pick the top layer of the garment. The step where the top layer is to be picked is indicated in purple (see accompanying video for further details).

action plan, however, correctly identified the layer fold (pick location marked in purple) as a fold where it had to pick the top layer. Therefore, methods that are specialized in performing a layered cloth picking could be integrated into our system, which we leave for future work.

X. CONCLUSIONS

In this work, we presented an extended version of the Latent Space Roadmap first introduced in [9] which allows visual action planning of manipulation tasks. Firstly, we improved the building procedure of the LSR in the latent space by introducing an outer optimization loop that eliminates the need for a hard-to-tune clustering parameter. We compared an extensive arsenal of clustering algorithms in our LSR building algorithm, and showed that the average linkage algorithm is best suited for the presented tasks. Secondly, we improved the training procedure of the VAE, used to represent the Mapping Module, by dynamically increasing the desired distance between action pairs. We thoroughly investigated the structure of the latent space, and presented a deep insight into the effects that each of the improvements have for the system. In addition, we compared different realizations of the Action Proposal Module and showcased the benefits of using latent representations for generating action plans. Lastly, we evaluated the new Latent Space Roadmap on both simulated box stacking task as well

as real-world folding task. We introduced a harder version of the box stacking task, which enabled a more informative ablation study. We showed that the improved LSR significantly outperforms the one presented in [9] on the same folding task.

We are convinced that in order to improve the state-of-the-art manipulation techniques for rigid and deformable objects, improvements on two fronts are necessary: learning a structured latent space as well as its exploration. We believe that our proposed method is a step toward achieving this goal.

REFERENCES

- [1] J. Oh, X. Guo, H. Lee, R. L. Lewis, and S. Singh, “Action-conditional video prediction using deep networks in atari games,” in *Advances in neural information processing systems*, pp. 2863–2871, 2015.
- [2] J. Sanchez, J.-A. Corrales, B.-C. Bouzgarrou, and Y. Mezouar, “Robotic manipulation and sensing of deformable objects in domestic and industrial applications: a survey,” *Int. J. Robot. Res.*, vol. 37, no. 7, pp. 688–716, 2018.
- [3] I. Garcia-Camacho, M. Lippi, M. C. Welle, H. Yin, R. Antonova, A. Varava, J. Borras, C. Torras, A. Marino, G. Alenyà, and D. Kragic, “Benchmarking bimanual cloth manipulation,” *IEEE Robot. Autom. Lett.*, vol. 5, no. 2, pp. 1111–1118, 2020.
- [4] D. H. Ballard, “Modular learning in neural networks,” in *AAAI*, pp. 279–284, 1987.
- [5] M. A. Kramer, “Nonlinear principal component analysis using autoassociative neural networks,” *AIChe journal*, vol. 37, no. 2, pp. 233–243, 1991.
- [6] D. P. Kingma and M. Welling, “Auto-encoding variational bayes,” *Int. Conf. Learn. Represent.*, 2015.
- [7] D. J. Rezende, S. Mohamed, and D. Wierstra, “Stochastic backpropagation and approximate inference in deep generative models,” in *Int. Conf. Mach. Learn.*, pp. 1278–1286, 2014.
- [8] D. Müllner, “Modern hierarchical, agglomerative clustering algorithms,” *arXiv preprint arXiv:1109.2378*, 2011.
- [9] M. Lippi, P. Poklukar, M. C. Welle, A. Varava, H. Yin, A. Marino, and D. Kragic, “Latent space roadmap for visual action planning of deformable and rigid object manipulation,” in *IEEE/RSJ Int. Conf. on Intelligent Robots and Systems*, 2020.
- [10] T. Lozano-Pérez and L. P. Kaelbling, “A constraint-based method for solving sequential manipulation planning problems,” in *IEEE/RSJ Int. Conf. on Intelligent Robots and Systems*, pp. 3684–3691, IEEE, 2014.
- [11] C. Galindo, J.-A. Fernández-Madriral, J. González, and A. Saffiotti, “Robot task planning using semantic maps,” *Robotics and Autonomous Systems*, vol. 56, no. 11, pp. 955 – 966, 2008. Semantic Knowledge in Robotics.
- [12] L. P. Kaelbling and T. Lozano-Pérez, “Integrated task and motion planning in belief space,” *Int. J. Robot. Res.*, vol. 32, no. 9-10, pp. 1194–1227, 2013.
- [13] S. M. LaValle, *Planning Algorithms*. Cambridge U.K.: Cambridge University Press, 2006.
- [14] R. Bellman, “Curse of dimensionality,” *Adaptive control processes: a guided tour*. Princeton, NJ, vol. 3, p. 2, 1961.
- [15] A. Srinivas, A. Jabri, P. Abbeel, S. Levine, and C. Finn, “Universal planning networks,” in *Int. Conf. Mach. Learn.*, 2018.
- [16] B. Jia, Z. Pan, Z. Hu, J. Pan, and D. Manocha, “Cloth manipulation using random-forest-based imitation learning,” *IEEE Robot. Autom. Lett.*, vol. 4, no. 2, pp. 2086–2093, 2019.
- [17] A. H. Qureshi, Y. Miao, A. Simeonov, and M. C. Yip, “Motion planning networks: Bridging the gap between learning-based and classical motion planners,” *IEEE Trans. Robot.*, pp. 1–19, 2020.
- [18] E. Todorov, T. Erez, and Y. Tassa, “Mujoco: A physics engine for model-based control,” in *IEEE/RSJ Int. Conf. on Intelligent Robots and Systems*, pp. 5026–5033, IEEE, 2012.
- [19] B. Ichter and M. Pavone, “Robot Motion Planning in Learned Latent Spaces,” *IEEE Robot. Autom. Lett.*, vol. 4, no. 3, pp. 2407–2414, 2019.
- [20] D. Hafner, T. Lillicrap, I. Fischer, R. Villegas, D. Ha, H. Lee, and J. Davidson, “Learning latent dynamics for planning from pixels,” in *Int. Conf. Mach. Learn.*, pp. 2555–2565, 2019.
- [21] A. Wang, T. Kurutach, P. Abbeel, and A. Tamar, “Learning robotic manipulation through visual planning and acting,” in *Robotics: Science and Systems*, 2019.
- [22] T. Kurutach, A. Tamar, G. Yang, S. J. Russell, and P. Abbeel, “Learning plannable representations with causal infogan,” in *Advances in Neural Information Processing Systems*, pp. 8733–8744, 2018.
- [23] A. Nair, D. Chen, P. Agrawal, P. Isola, P. Abbeel, J. Malik, and S. Levine, “Combining self-supervised learning and imitation for vision-based rope manipulation,” in *IEEE Int. Conf. Robot. Autom.*, pp. 2146–2153, 2017.
- [24] K. Pertsch, O. Rybkin, F. Ebert, C. Finn, D. Jayaraman, and S. Levine, “Long-horizon visual planning with goal-conditioned hierarchical predictors,” 2020.
- [25] C. Finn and S. Levine, “Deep visual foresight for planning robot motion,” in *IEEE Int. Conf. Robot. Autom.*, pp. 2786–2793, 2017.
- [26] T. Kipf, E. van der Pol, and M. Welling, “Contrastive learning of structured world models,” in *Int. Conf. Learn. Represent.*, 2020.
- [27] B. Eysenbach, R. R. Salakhutdinov, and S. Levine, “Search on the replay buffer: Bridging planning and reinforcement learning,” in *Advances in Neural Information Processing Systems*, pp. 15246–15257, 2019.
- [28] R. Hadsell, S. Chopra, and Y. LeCun, “Dimensionality reduction by learning an invariant mapping,” in *IEEE Computer Society Conf. on Computer Vision and Pattern Recognition*, vol. 2, pp. 1735–1742, 2006.
- [29] I. Higgins, L. Matthey, A. Pal, C. Burgess, X. Glorot, M. Botvinick, S. Mohamed, and A. Lerchner, “ β -vae: Learning basic visual concepts with a constrained variational framework,” *Int. Conf. Learn. Represent.*, 2017.
- [30] C. P. Burgess, I. Higgins, A. Pal, L. Matthey, N. Watters, G. Desjardins, and A. Lerchner, “Understanding disentangling in β -vae,” *arXiv preprint arXiv:1804.03599*, 2018.
- [31] R. R. Sokal, “A statistical method for evaluating systematic relationships,” *Univ. Kansas. Sci. Bull.*, vol. 38, pp. 1409–1438, 1958.
- [32] M. E. Celebi, *Partitional clustering algorithms*. Springer, 2014.
- [33] C. C. Aggarwal and C. K. Reddy, “Data clustering,” *Algorithms and applications*. Chapman&Hall/CRC Data mining and Knowledge Discovery series, Londra, 2014.
- [34] P. Langfelder, B. Zhang, and S. Horvath, “Defining clusters from a hierarchical cluster tree: the dynamic tree cut package for r,” *Bioinformatics*, vol. 24, no. 5, pp. 719–720, 2008.
- [35] D. Bruzese and D. Vistocco, “Despota: Dendrogram slicing through a permutation test approach,” *J. Classif.*, vol. 32, no. 2, pp. 285–304, 2015.
- [36] A. Pasini, E. Baralis, P. Garza, D. Floriello, M. Idiommi, A. Ortenzi, and S. Ricci, “Adaptive hierarchical clustering for petrographic image analysis,” in *EDBT/ICDT Workshops*, 2019.
- [37] R. P. Brent, “An algorithm with guaranteed convergence for finding a zero of a function,” *The Computer Journal*, vol. 14, no. 4, pp. 422–425, 1971.
- [38] A. A. Hagberg, D. A. Schult, and P. J. Swart, “Exploring Network Structure, Dynamics, and Function using NetworkX,” in *Python in Science Conf.*, pp. 11–15, 2008.
- [39] Unity Technologies, “Unity.”
- [40] K. He, X. Zhang, S. Ren, and J. Sun, “Deep residual learning for image recognition,” in *IEEE Conf. on Computer Vision and Pattern Recognition*, pp. 770–778, 2016.
- [41] C. C. Aggarwal, A. Hinneburg, and D. A. Keim, “On the surprising behavior of distance metrics in high dimensional space,” in *Int. Conf. Database Theory*, pp. 420–434, Springer, 2001.
- [42] K. Beyer, J. Goldstein, R. Ramakrishnan, and U. Shaft, “When is “nearest neighbor” meaningful?,” in *Int. Conf. Database Theory*, pp. 217–235, Springer, 1999.
- [43] D. Berthelot, C. Raffel, A. Roy, and I. Goodfellow, “Understanding and improving interpolation in autoencoders via an adversarial regularizer,” *arXiv preprint arXiv:1807.07543*, 2018.
- [44] A. Oring, Z. Yakhini, and Y. Hel-Or, “Faithful autoencoder interpolation by shaping the latent space,” *arXiv preprint arXiv:2008.01487*, 2020.
- [45] M. Ester, H.-P. Kriegel, J. Sander, X. Xu, et al., “A density-based algorithm for discovering clusters in large spatial databases with noise,” in *Kdd*, vol. 96, pp. 226–231, 1996.
- [46] L. Ertöz, M. Steinbach, and V. Kumar, “Finding clusters of different sizes, shapes, and densities in noisy, high dimensional data,” in *SIAM Int. Conf. Data Mining*, pp. 47–58, SIAM, 2003.
- [47] Y. Cheng, “Mean shift, mode seeking, and clustering,” *IEEE Trans. Pattern. Anal. Mach. Intell.*, vol. 17, no. 8, pp. 790–799, 1995.
- [48] F. Pedregosa, G. Varoquaux, A. Gramfort, V. Michel, B. Thirion, O. Grisel, M. Blondel, P. Prettenhofer, R. Weiss, V. Dubourg, J. Vanderplas, A. Passos, D. Cournapeau, M. Brucher, M. Perrot, and E. Duchesnay, “Scikit-learn: Machine learning in Python,” *J. Mach. Learn. Res.*, vol. 12, pp. 2825–2830, 2011.
- [49] M. Ankerst, M. M. Breunig, H.-P. Kriegel, and J. Sander, “Optics: ordering points to identify the clustering structure,” *ACM Sigmod record*, vol. 28, no. 2, pp. 49–60, 1999.

- [50] R. J. Campello, D. Moulavi, and J. Sander, “Density-based clustering based on hierarchical density estimates,” in *Pacific-Asia Conf. on Knowledge Discovery and Data Mining*, pp. 160–172, Springer, 2013.
- [51] W. H. Day and H. Edelsbrunner, “Efficient algorithms for agglomerative hierarchical clustering methods,” *J. Classif.*, vol. 1, no. 1, pp. 7–24, 1984.
- [52] L. McInnes, J. Healy, and S. Astels, “hdbscan: Hierarchical density based clustering,” *The Journal of Open Source Software*, vol. 2, no. 11, p. 205, 2017.
- [53] A. Krizhevsky, “Learning multiple layers of features from tiny images,” tech. rep., 2009.
- [54] C. Burgess and H. Kim, “3d shapes dataset,” <https://github.com/deepmind/3dshapes-dataset/>, 2018.
- [55] D. Seita, A. Ganapathi, R. Hoque, M. Hwang, E. Cen, A. K. Tanwani, A. Balakrishna, B. Thananjeyan, J. Ichnowski, N. Jamali, K. Yamane, S. Iba, J. Canny, and K. Goldberg, “Deep Imitation Learning of Sequential Fabric Smoothing From an Algorithmic Supervisor,” in *IEEE/RSJ Int. Conf. on Intelligent Robots and Systems*, 2020.

APPENDIX

This section provides complementary results to the box stacking task.

1) Comparing VAE and AE: Table XIII shows the LSR performance, evaluated on full scoring, of the AE compared to the VAE on the normal stacking task using metric L_1 and $ld = 12$. It shows that, as for the hard stacking task, the probabilistic approach of the VAE is better suited for visual action planning than the deterministic approach of AE also on the easier task. When using AE- L_1 , we obtained an average performance of 80.2% on partial scoring (column % Any), while perfect performance was achieved with the VAE framework. The table also validates the effectiveness of the action loss which allows to increase the performance from 20.5% to 80.2% even in the AE formulation.

Model	% All	% Any	% Trans.
AE- b +LSR- L_1	16.0 ± 5.0	20.5 ± 5.8	79.9 ± 2.1
AE- L_1 +LSR- L_1	76.0 ± 9.1	80.2 ± 7.6	94.1 ± 2.0
VAE- L_1 +LSR- L_1	100.0 ± 0	100.0 ± 0	100.0 ± 0

Table XIII: LSR performance comparison on the normal stacking task using VAE and AE. Best results in bold.

2) Comparing different metrics: As in our previous work [9], we also analyzed the influence of using different distance metrics in both the action loss term (4) and LSR building algorithm summarized in Algorithm 1.

Table XIV reports the LSR results on partial scoring when using different metrics for both the VAE and the LSR in the normal (on the left) and the hard (on the right) box stacking tasks. Firstly, we observe that for both tasks we obtained significantly worse LSR performance when using the baseline VAEs (VAE- b) compared to the action VAEs.

Secondly, we observe that the best performance was achieved with VAE- L_1 + LSR- L_1 and the worst using VAE- L_∞ + LSR- L_∞ , which is consistent with our earlier experiments [9]. Note that this behavior is much more evident on the hard box stacking task. As supported by [41], we hypothesise that this is because L_1 metric is calculated as the sum of the absolute differences between the individual coordinates and hence the points need to be evenly separated with respect to all dimensions. On the contrary, L_∞ separates points based on only one dimension which leads to erroneous merges as two points might be far apart with respect to one dimension but

very close with respect to the rest. Finally, we again observed differences in performance between ns and hs which reflect the difficulty level of the tasks: an average value of 92.1% for the existence of at least one correct path was achieved for hs , while 100% was achieved for ns . In summary, this experiment reproduces results obtained in our previous work [9] and shows a superior performance when using distance metric L_1 both in the action loss and in the LSR building.

Model	ns [%]	hs [%]
VAE- b +LSR- L_1	4.1 ± 1.0	0.2 ± 0.1
VAE- b +LSR- L_2	2.3 ± 1.0	0.3 ± 0.3
VAE- b +LSR- L_∞	0.5 ± 0.4	0.1 ± 0.1
VAE- L_1 +LSR- L_1	100.0 ± 0	92.1 ± 2.9
VAE- L_2 +LSR- L_2	96.7 ± 4.1	62.3 ± 9.3
VAE- L_∞ +LSR- L_∞	82.7 ± 15.9	18.3 ± 3.4

Table XIV: LSR performance (partial scoring) for the normal (left) and hard (right) box stacking tasks comparing different metrics. Best results in bold.

3) Comparing different clustering algorithms for LSR:

Table XV shows the comparison of different clustering algorithms in the normal box stacking task using VAE $_{12-ns}$ - L_1 . In particular, we report the results obtained when performing a grid search (left column) and when performing the automatic optimization to determine the respective algorithm parameter as described in Sec. VI-B (right column). All the clustering algorithms lead to optimal performance with the grid search, except for the OPTICS which achieved an average performance of 94.2%. This result again demonstrates that the hard version of the box stacking task is much more complex than the normal one. Moreover, this experiment validates the optimization procedure described in Algorithm 2 since average performance greater than 99.7% was recorded for all methods except for OPTICS where we obtained 91.1%.

It is worth remarking that it is generally not possible to perform grid search since the ground truth is generally not known, as for example in the folding task.

Clust. method	Grid Search [%]	Optimization [%]
Epsilon [9]	100.0 ± 0.0	100.0 ± 0.0
Meanshift	100.0 ± 0.0	99.7 ± 0.6
OPTICS	94.2 ± 2.5	91.1 ± 3.6
HDBSCAN	100.0 ± 0.0	-
Single-linkage	100.0 ± 0.0	100.0 ± 0.0
Complete-linkage	100.0 ± 0.0	100.0 ± 0.0
Average-linkage	100.0 ± 0.0	100.0 ± 0.0

Table XV: LSR performance comparison of different clustering algorithms in the normal box stacking task. Partial scoring when applying grid search (left column) and when using the optimization in Algorithm 2 (right column) is shown. Best results in bold.